



Anomalous low aftershock productivity of the 2019 M_W 8.0 energetic intermediate-depth faulting beneath Peru

Lingling Ye ^{a,*}, Thorne Lay ^b, Hiroo Kanamori ^c

^a Guangdong Provincial Key Lab of Geodynamics and Geohazards, School of Earth Sciences and Engineering, Sun Yat-sen University, Guangzhou, China

^b Department of Earth and Planetary Sciences, University of California Santa Cruz, Santa Cruz, CA 95064, USA

^c Seismological Laboratory, California Institute of Technology, Pasadena, CA 91125, USA

ARTICLE INFO

Article history:

Received 16 March 2020
Received in revised form 23 June 2020
Accepted 13 August 2020
Available online xxxxx
Editor: R. Bendick

Keywords:

intermediate-depth earthquakes
2019 Peru earthquake
aftershock productivity
flat slab
stress heterogeneity

ABSTRACT

The 26 May 2019 Peru (M_W 8.0) earthquake struck within the nearly-horizontal underthrust Nazca plate at depths from ~ 110 to 150 km below the upper Amazon, near a steep bend in the plate where it plunges down to a deep earthquake zone. Little prior seismicity occurred in this region, but large intraslab events with similar normal-faulting mechanisms have occurred to the west. The event is situated in a similar slab position to the 2017 Puebla-Morelos, Mexico earthquake, but the remote location resulted in limited loss of life and damage. Back-projection imaging and finite-fault inversion based on teleseismic data suggest a brittle and energetic rupture process with unilateral expansion northward over a 170-km-long zone at a rupture speed, $V_r \sim 3$ km/s, with three normal-faulting patches of up to ~ 4.5 m slip. Despite the mainshock size, it produced only three $M_{4.0+}$ aftershocks within 300 km (one nearby); the aftershock productivity of the 2019 Peru earthquake is very low even among all large intermediate-depth earthquakes, but similar to that for other large Peruvian intraslab events. Comparison of aftershock productivity of the Peru event with that of global large earthquakes in various tectonic settings suggests that the low aftershock productivity can largely be attributed to regionally homogeneous faulting systems and relatively uniform stress state in the flat Peru slab.

© 2020 Published by Elsevier B.V.

1. Introduction

Intermediate-depth earthquakes occur within underthrust oceanic slabs, and large events from 70 to ~ 150 km deep can be particularly damaging because they locate inland beneath populated coastlines (e.g., Delouis and Legrand, 2007; McCloskey et al., 2010; Ye et al., 2014, 2017; Melgar et al., 2018). The nature of intermediate-depth earthquakes is debated; various studies attribute their occurrence at depths where ductile deformation should dominate to dehydration embrittlement of serpentinite, antigorite serpentinite, or lawsonite (e.g., Raleigh and Paterson, 1965; Green and Houston, 1995; Kirby et al., 1996; Peacock, 2001; Hacker et al., 2003; Jung et al., 2004; Okazaki and Hirth, 2016), or shear-heating in viscous shear zones and thermal shear runaway (e.g., Ogawa, 1987; Hobbs and Ord, 1988; Kelemen and Hirth, 2007; John et al., 2009; Prieto et al., 2013). Localized hydration of the subducting slab is commonly attributed to fluid penetration along outer rise extensional faults formed during slab bending (e.g., Ranero et al., 2005; Faccenda et al., 2009; Emry et al., 2014;

Shiina et al., 2017). Hydrated minerals concentrated along these pre-existing faults can then destabilize at depth, with released fluid increasing pore pressures and reducing effective stress to allow brittle shear failure of the strengthened matrix in response to slab stresses at intermediate depth. The faulting is essentially indistinguishable from shallower earthquakes. Seismologists continue to seek characteristics of either sources (e.g., Houston et al., 1998; Campus and Das, 2000; Tibi et al., 2002; Prieto et al., 2013; Ye et al., 2014; Twardzik and Ji, 2015) or seismic sequences (e.g., Wiens and Gilbert, 1996; Wiens et al., 1997; Wiemer and Benoit, 1996) that can help to resolve the nature of intermediate-depth earthquakes.

On 26 May 2019, a great earthquake (M_W 8.0, m_b 7.3) struck below the upper Amazon region of eastern Peru (U.S. Geological Survey National Earthquake Information Center (USGS-NEIC), 07:41:15 UTC, 5.812°S, 75.270°W, 122.6 km; <https://earthquake.usgs.gov/earthquakes/eventpage/us60003sc0/executive>). The earthquake ranks among the top ten largest intermediate-depth events in the seismological record (Astiz et al., 1988; Ye et al., 2014), and is the largest intermediate-depth earthquake with modern broadband seismological recordings. It is located within a flat portion of the subducted Nazca slab extending eastward beneath Peru

* Corresponding author.

E-mail address: yelingling@mail.sysu.edu.cn (L. Ye).

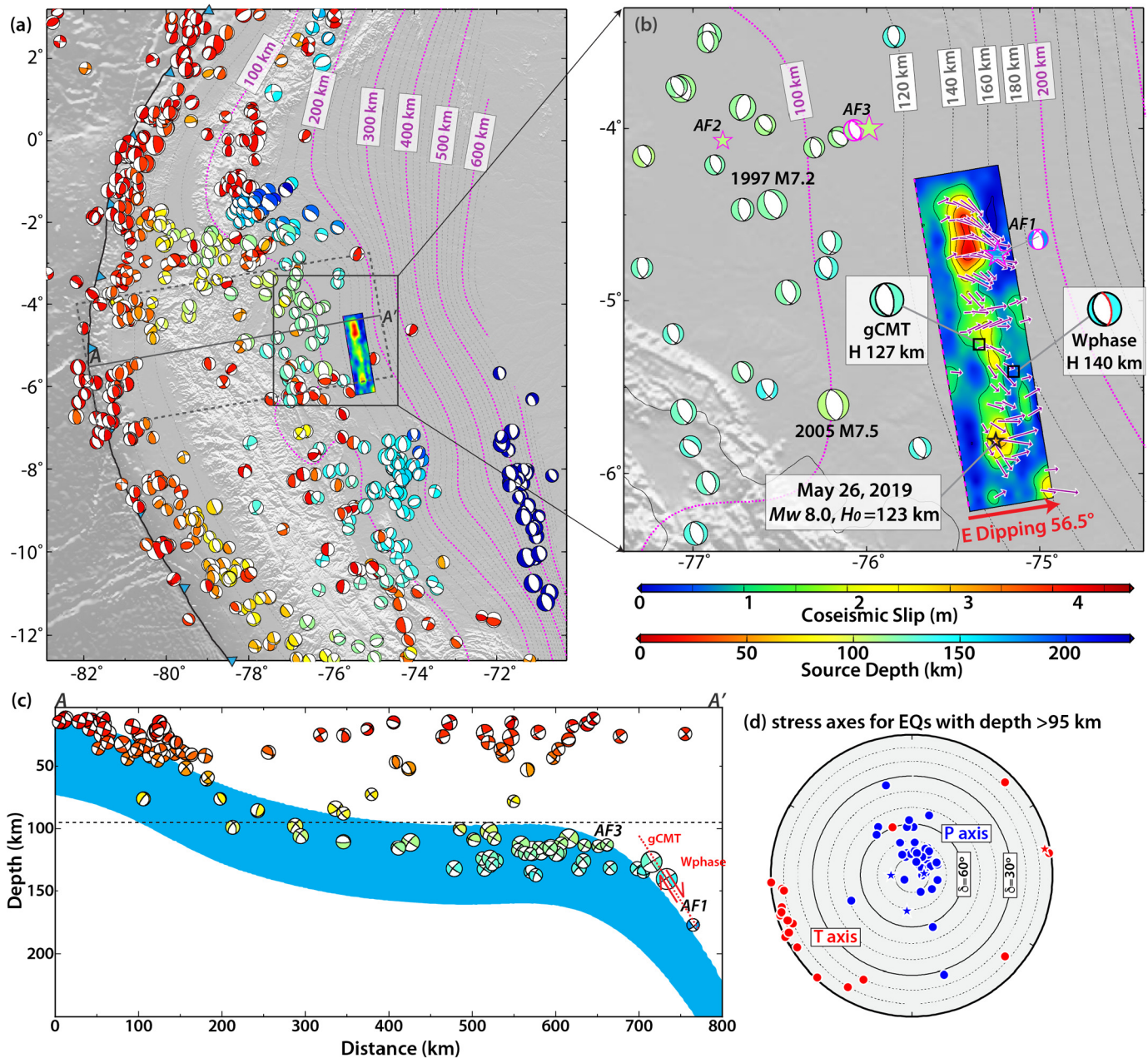


Fig. 1. (a) Fault mechanisms from the gCMT catalog during 1976 to 2019 under northern Peru, Ecuador and western Brazil, color-coded with source depth. (b) Slip distribution of the 26 May 2019 M_W 8.0 earthquake, along with the gCMT and W-phase focal mechanisms. Three intermediate-depth aftershocks within one month are marked as AF1 (5/29, USGS-NEIC depth 150.9 km, M4.8; gCMT centroid depth 176.9 km), AF2 (6/15, USGS-NEIC depth 108.5 km, M4.4) and AF3 (6/19, USGS-NEIC depth 107.4 km, M4.9; gCMT centroid depth 113.3 km), respectively. The magenta- and black-dashed curves are 20 km depth contours of the slab interface from Slab2 (Hayes et al., 2018). (c) A vertical cross-section of model Slab2 (blue area) in central Peru along the direction of A-A' and gCMT focal mechanisms since 1976 in the dashed box in (a). The red dashed line approximates the depth extent of the mainshock rupture. (d) Lower-hemisphere projection of compressional (P, blue) and extensional (T, red) gCMT principal stress orientations for events with depth larger than 95 km in (c). Stars are for the 2019 M_W 8.0 Peru earthquake and aftershocks (AF1 and AF3). Note the uniformity of principle stress orientations in the flat slab around the 2019 Peru earthquake. (For interpretation of the colors in the figure(s), the reader is referred to the web version of this article.)

prior to the slab plunging steeply with little seismicity from 250 to 600 km depth to a deep earthquake zone (Figs. 1 and S1). The 2019 Peru earthquake was widely felt, but the far-inland location limited the damage to 2 fatalities and 30 injuries along with 404 homes destroyed (<https://reliefweb.int/report/peru/peru-earthquake-number-affected-houses-rises-833-404-uninhabitable>). The focal mechanism has a nearly horizontal tension axis trending N78°E, similar to other large events westward in the horizontal slab (Fig. 1b). The USGS-NEIC detected no foreshocks and only three intermediate-depth aftershocks within 300 km within one month after the event. This constitutes very low aftershock pro-

ductivity given the mainshock size, even for an intermediate-depth earthquake.

To achieve a better understanding of the nature of intermediate-depth faulting, we determine the rupture process of the 2019 Peru earthquake using back-projection imaging and finite-fault modeling with teleseismic data, and compare the spatio-temporal rupture evolution with regional faulting and seismicity patterns. The low aftershock productivity is considered in the context of the slip distribution, the slab thermal parameter, aftershock productivity of global large earthquakes, and the regional intermediate-depth faulting in the nearly-horizontal Peru slab.

2. Mainshock rupture properties

2.1. Long-period point-source solutions

Long-period seismic point-source inversions for the 2019 Peru earthquake show consistent, predominantly double-couple focal mechanisms, with minor non-double-couple (NDC) component which, for other deep and intermediate-depth earthquakes, has been attributed to possible multiple-fault rupture or anisotropic slab structure near the source (e.g., Kuge and Kawakatsu, 1993; Li et al., 2018). Using 383 body-wave and 292 surface-wave displacements filtered between 50 s to 150 s and 498 mantle waves filtered between 150 s to 400 s, the global centroid moment tensor (gCMT) solution (<http://www.globalcmt.org/CMTsearch.html>; Ekström et al., 2012) has major double-couple nodal planes with strike $\phi_1 = 351^\circ$, dip $\delta_1 = 57^\circ$, rake $\lambda_1 = -87^\circ$, and $\phi_2 = 166^\circ$, $\delta_2 = 33^\circ$, $\lambda_2 = -94^\circ$, centroid depth of 126.6 km, centroid time shift of 37.7 s, and seismic moment $M_0 = 1.23 \times 10^{21}$ Nm with 20% NDC component. The rapid *W*-phase solution from USGS-NEIC has a seismic moment $M_0 = 1.139 \times 10^{21}$ Nm (28% NDC component), centroid depth of 130.5 km, and two best-double-couple nodal planes with $\phi_1 = 350^\circ$, $\delta_1 = 53^\circ$, $\lambda_1 = -88^\circ$, and $\phi_2 = 166^\circ$, $\delta_2 = 37^\circ$, $\lambda_2 = -93^\circ$ (<https://earthquake.usgs.gov/earthquakes/eventpage/us60003sc0/moment-tensor>). We perform additional *W*-phase moment-tensor inversions (Kanamori and Rivera, 2008) using 186 signals filtered between 100 s to 600 s (Fig. S3), obtaining a solution with seismic moment $M_0 = 1.36 \times 10^{21}$ Nm (22% non-double-couple component), best double-couple nodal planes with strike $\phi_1 = 350.5^\circ$, dip $\delta_1 = 56.9^\circ$, rake $\lambda_1 = -85.0^\circ$, and $\phi_2 = 161.3^\circ$, $\delta_2 = 33.4^\circ$, $\lambda_2 = -97.7^\circ$, centroid depth of 140.5 km, and centroid time shift of 36 s (Fig. S2). These long-period point-source solutions all yield M_W 8.0 with near-vertical compressional and near-horizontal tensional stress orientations similar to focal mechanisms of prior intermediate-depth earthquakes in the flat Nazca plate beneath Peru (Fig. 1d), suggesting relatively uniform rupture and strain regime in this slab environment.

2.2. Back-projection imaging

To constrain rupture finiteness of the 2019 Peru earthquake, we performed back-projections (BPs) of high-frequency (HF) teleseismic *P* wave recordings from European and Alaskan stations (Fig. 2a) using the method of Xu et al. (2009). For large intermediate-depth earthquakes, the *P* wave time series include clear depth phases, which usually have long-period signals with large amplitude (Fig. 2b). Depending on the source-station geometry, depth phases show different move-out from direct *P* waves, resulting in artifacts in the BP images. To account for array response artifacts that smear the BP images along the great-circle directions to the networks, we performed three BPs of 0.5–2.0 Hz recordings with different source-station geometries using Alaskan, European and combined Alaskan and European networks. Albeit with smeared averaged beam power due to array responses, all BP images show northward unilateral rupture over at least 160 km in ~ 50 s with three discrete coherent HF beam peaks in 10–15 s, 20–25 s and ~ 40 –50 s time intervals, indicating an apparent rupture speed of ~ 3 km/s (Fig. 2d–2f). The consistent northward unilateral rupture, oblique to the great-circle directions, demonstrates that the HF beam peaks are mainly generated by the rupture rather than by depth phases, which are less coherent in the HF pass-band used (Fig. 2c). IRIS back-projections (<http://ds.iris.edu/spud/backprojection/17616500>) using large-aperture networks of North American and global stations with lower frequency bands of 0.25–1.0 Hz and 0.05–0.25 Hz respectively, and back-projection with a different stacking method by Liu and Yao (2020) for a frequency band of 0.5–2 Hz using stations in Alaska, show similar northward

rupture with three strong high-frequency radiation intervals, suggesting that this is a robust feature of the rupture.

2.3. Finite-fault slip inversion

Guided by the possible fault geometries from point-source solutions and rupture speed constraint from BP images, we inverted broadband teleseismic body waves for finite-fault models using a linear least-squares kinematic inversion with specified maximum rupture expansion speed and multiple subfault source time windows (Hartzell and Heaton, 1983; Kikuchi and Kanamori, 1991; Ye et al., 2016a). The preferred source model is for a nodal plane with strike 350.5° and dip 56.9° from our *W*-phase solution with an assumed maximum rupture expansion speed of 3 km/s (Fig. 3). We used 18 subfaults with 12 km spacing along strike and 11 subfaults with 9 km spacing along dip, and parameterized each subfault source time function with 18 overlapping triangles that can have variable rake with 2 s rise time shifted by 2 s, resulting in a maximum subfault slip duration of 38 s. The relatively long subfault rupture duration parameterization allows variation in the overall rupture propagation speed. The main slip pattern is similar if we use relatively short subfault source time functions prescribed by 7 triangles with 2.5 s rise time shifted by 2.5 s (Figs. S5 and S7b). The rupture starts at the USGS-NEIC hypocenter depth of 122.6 km. The structural model for the source region used in the inversion is the local model from Crust 1.0 (Laske et al., 2013) overlying the PREM model (Dziewonski and Anderson, 1981). We inverted 79 *P* and 37 *SH* displacement waveform trains filtered in the frequency band 0.005–0.9 Hz (Fig. 3e) with spatial smoothing and a total seismic moment constrained by our long-period *W*-phase solution (Ye et al., 2016a). We modified the inversion code to account for different attenuation effects between direct body waves and depth phases. We applied effective attenuation parameters $t^* = 0.75$ s for direct *P* wave and 3.0 s for direct *S* waves for waveform modeling, and $t^* = 1.5$ s, 3.0 s, 4.0 s and 5.0 s for pP, sP, pS and sS depth phases, respectively.

The alternative westward-dipping nodal plane with $\phi = 161.3^\circ$ and $\delta = 33.4^\circ$ with similar inversion parameterization can provide a comparable waveform match to that for eastward-dipping nodal plane. However, the slip distribution on the eastward-dipping fault is more straightforward to reconcile with the local aftershock location and BP beam peaks (Fig. 4): Coherent BP short-period energy bursts and the early aftershock (AF1) locate near the downdip edge of the three large-slip regions with similar source depth for the eastward-dipping fault plane, indicating that it is the likely rupture plane.

For our preferred eastward-dipping finite fault slip model, the seismic moment is $M_0 = 1.38 \times 10^{21}$ Nm, rupture duration is ~ 65 s and centroid time shift is 40 s (Fig. 3a). The inverted slip distribution, albeit having large grid size and spatial smoothing, also shows unilateral rupture with three discrete large-slip patches distributed ~ 170 km along strike (Figs. 3c, 4a–c). For the first 15 s, the rupture propagates radially from the hypocenter; most slip locates downdip over 20–30 km with peak slip of ~ 3.2 m. Then the rupture expands northward uniformly with a slip patch 40–80 km from the hypocenter at ~ 25 s. The largest slip patch is ~ 110 –150 km north from the hypocenter, with peak slip of ~ 4.5 m and peak moment-rate of 8×10^{19} Nm/s. The large-slip patches are limited to a depth range of ~ 110 –150 km, based on the good predictions of *P* and *SH* waveform and corresponding depth phases (Fig. 3e); the centroid source depth for this model is ~ 130 km, consistent with point-source estimates from long-period seismic waveforms.

As is typical of teleseismic-only inversions, there is a trade-off between rupture expansion speed and rupture spatial distribution for the finite-fault inversion, but the northward directivity is well-resolved. The overall consistency between the main slip patches in

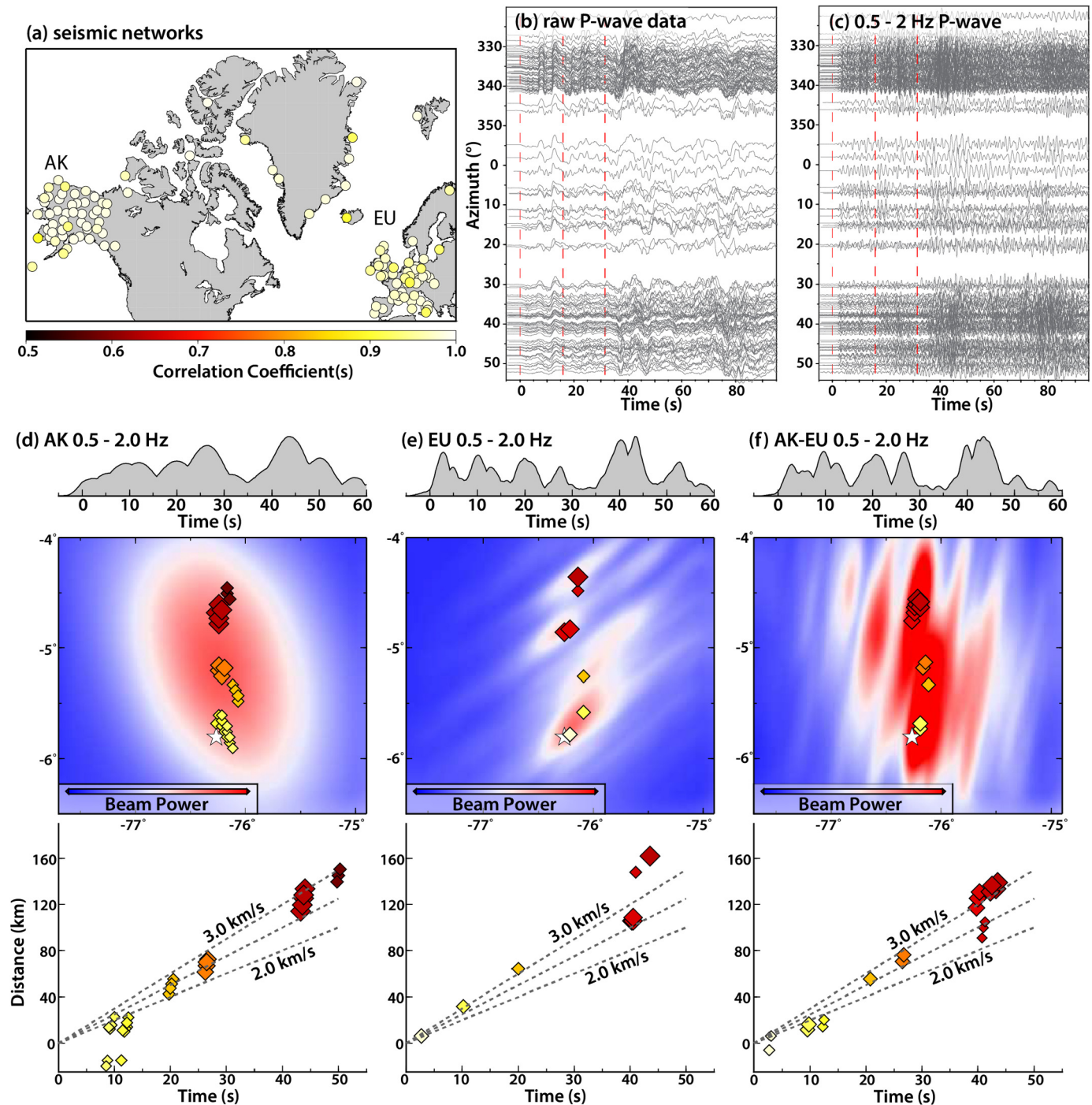


Fig. 2. Back-projection (BP) of short-period *P* waves from stations in Alaskan and European networks for the 2019 M_W 8.0 Peru earthquake. (a) Multiple channel correlation coefficients (MCCC) for *P* waveforms from 3 s before to 3 s after predicted *P* arrivals for all seismic stations used. (b) Broadband *P* waveforms aligned by MCCC. (c) *P* waves filtered in the 0.5-2.0 Hz passband used in BP imaging. (d-f) Top panel: stacked beam power versus time for Alaskan (d), European (e), and combined Alaska and European (f) networks. Middle panel: Locations of discrete coherent high-frequency beam peaks (diamonds, color-coded for lapse time after the origin time) superimposed on the time-averaged stack beam power imaged by back-projection of short-period *P* waves in each network. Lower Panel: distance of the coherent high-frequency bursts from the epicenter (white star in the map) versus lapse time, indicating that the average rupture speed of the 2019 Peru earthquake is ~ 3 km/s.

our preferred slip model and coherent BP beam peaks shown in Fig. 4a-c suggests that our model parameterization is reasonable. Fig. 3d shows the distribution of stress change with a peak value of ~ 16.5 MPa. The slip-weighted average stress drop $\Delta\sigma_E$ (Ye et al., 2016a) is 5.2 MPa. Trimming of subfaults with seismic moment $< 15\%$ of the peak subfault moment, the effective rupture area is $12,960 \text{ km}^2$ and average slip is 1.5 m. The associated area-based static stress drop, assuming a circular rupture, $\Delta\sigma_{0.15}$ is 2.3 MPa. The stress drop estimates are comparable to some intraslab earth-

quakes such as the 2013 M_W 8.3 Sea of Okhotsk deep event (Ye et al., 2013) and the first M_W 7.5 event in the 2015 Peru deep doublet event (Ye et al., 2016b), but smaller than the 2014 Rat Island M_W 7.9 intermediate-depth earthquake $\Delta\sigma_E = 16 - 25$ MPa (Ye et al., 2014) and the second M_W 7.6 event in the 2015 Peru deep doublet event (Ye et al., 2016b).

Usually, the parameterization in finite-fault inversions has a strong influence on stress drop calculation, and most finite-fault inversions likely underestimate true stress drop (Ye et al., 2016a).

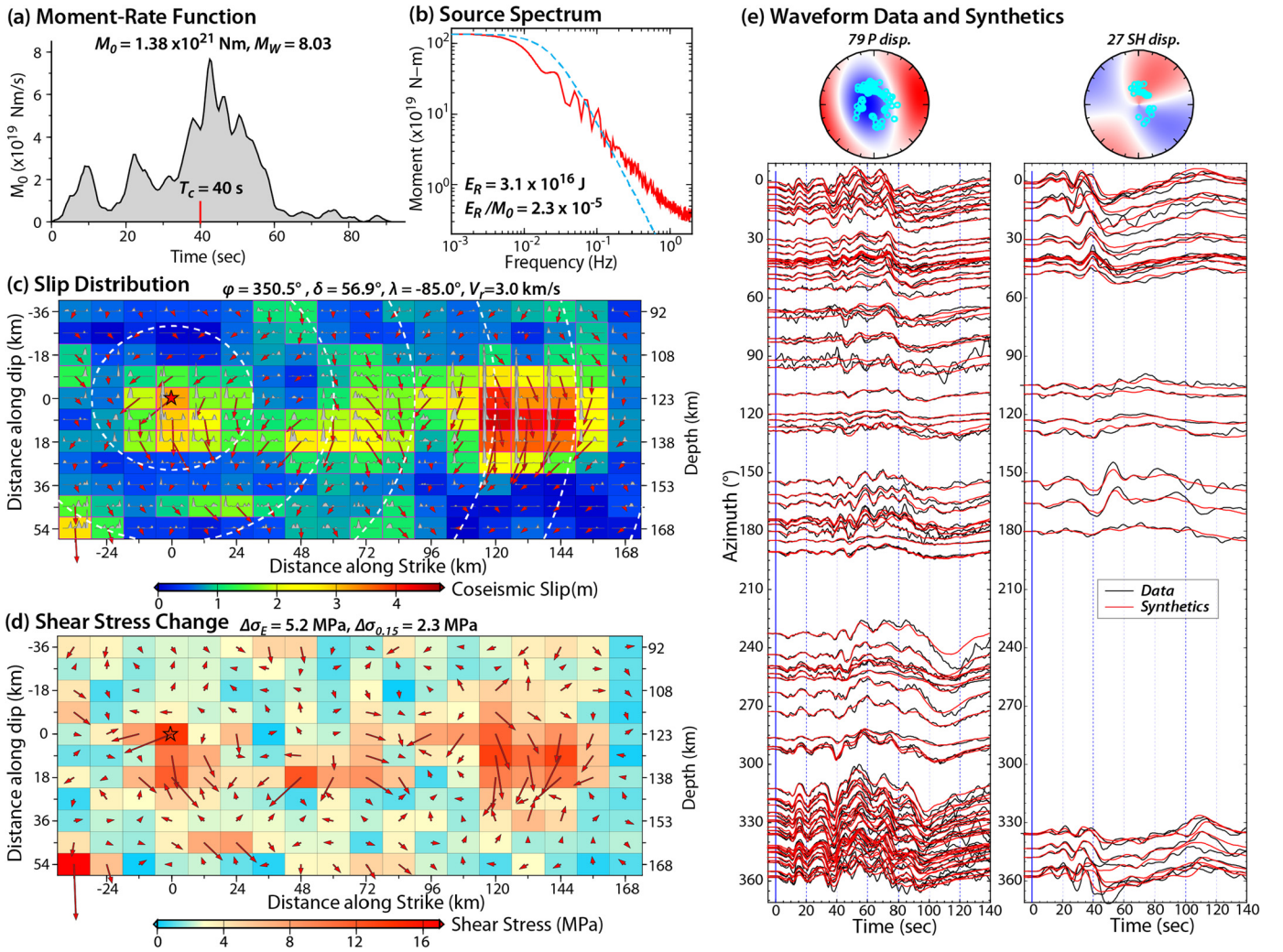


Fig. 3. Finite-fault rupture model for the 2019 M_W 8.0 Peru earthquake obtained from inversion of teleseismic P and SH waves. (a) The moment-rate function, with a red tick at the centroid time T_c . (b) Source spectrum inferred from the moment-rate function and teleseismic P spectra. (c) Slip distribution, with arrows showing the magnitude and direction of slip (hanging-wall relative to foot-wall) and subfaults color-coded by peak slip. The dashed blue curves indicate the positions of the rupture expansion front in 10 s intervals. The subfault source time functions are shown within each subfault by gray polygons. (d) Shear stress change calculated from the slip distribution in the half space (Okada, 1985). (e) Lower-hemisphere stereographic projections of the P -wave (left) and SH -wave (right) radiation patterns with raypath take-off positions for the data used in the inversion and comparisons of the observed (black) and predicted (red) waveforms for this model.

To evaluate the influence from the parameterization, we performed an inversion with relatively short parameterized subfault source functions prescribed by 7 triangles with 2.5 s rise time shifted by 2.5 s (Fig. S5) and another inversion with relatively smaller grid size for each subfault with 6 km spacing both along strike and along dip (Fig. S6). Compared with our preferred model shown in Figs. 4 and S4, all three models show similar spatial extent of rupture expansion (Fig. S7), consistent with BP images. The two models with same size of subfaults give similar slip-weighted stress drop and area-based stress drop (Figs. S7a and S7b). Slip-weighted stress drop is usually scaled up for models with small grids (e.g., Ye et al., 2016a; Adams et al., 2019), and it is 12.7 MPa for the model with 6 km spacing. However, the area-based stress drop, which provides a lower bound of stress drop in finite source models, is relatively stable, and the value is 3.3 MPa for the model with 6 km spacing. This is consistent with the similarity in the spatial pattern of slip distribution (Fig. S7), suggesting that the inference of strong unilateral expansion northward is robust.

The local rise time, or slip duration, is not well resolved from the finite-fault inversion with only teleseismic data. For models with 12-km spacing along strike and 9-km spacing along dip, local slip duration and local centroid time for subfaults in the main

slip area are about 10–15 s and 3–5 s, respectively (Figs. S4 and S5). The local slip duration and local centroid time are halved for the model with 6-km spacing about along strike and along dip, indicating that the subfault slip duration is mainly controlled by the propagation effect within each subfault, and the point slip rise time in the main slip area is shorter than the slip duration of 5–10 s in each 6-km long subfault. This suggests the rupture process in the 2019 Peru earthquake is probably slip pulse-like.

We estimate the average source spectrum for the 2019 Peru earthquake by combining the moment-rate spectrum for frequencies <0.05 Hz with stack-average broadband P wave displacement spectra at >0.05 Hz corrected for radiation pattern, geometrical spreading and attenuation with $t^* = 0.75$ s. Compared to a reference ω^{-2} source spectrum with a stress parameter of 3 MPa, the source radiation for the 2019 Peru event is slightly depleted in 0.01–0.1 Hz signal, but slightly enriched in high frequency radiation (Fig. 4b). Integrated from 0.0 to 1.0 Hz, the total radiated energy $E_R = 3.1 \times 10^{16}$ J, using $t^* = 0.75$ s. This value agrees well with the IRIS broadband radiated energy measure, $E_R = 3.4 \times 10^{16}$ J, from a different method (<http://ds.iris.edu/spud/eqenergy/17616740>). Our seismic moment-scaled radiated energy $E_R/M_0 = 2.3 \times 10^{-5}$, is comparable to other deep events and shallow intraslab events

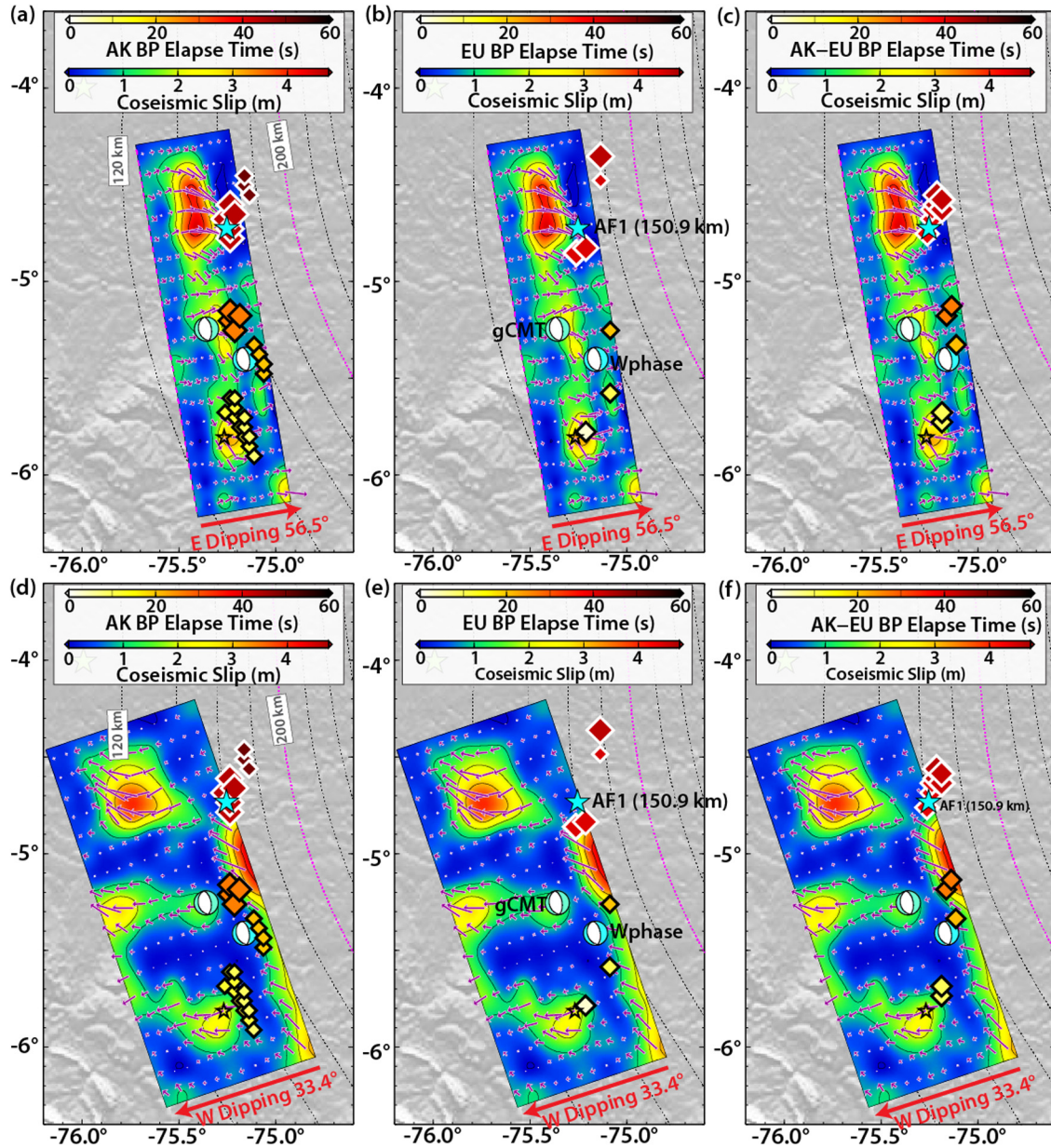


Fig. 4. (a-c) Comparison of the slip distribution on the eastward-dipping fault plane (Fig. 3) with BP images from the AK (left), EU (middle), and combined AK and EU (right) network data, along with aftershock $AF1$ epicenter and mainshock centroid point-source locations from gCMT and W-phase solutions. (d-f) Similar plots for the slip distributions on the westward-dipping nodal plane with strike of 161.3° .

(Ye et al., 2014, 2016b; Meng et al., 2015). The estimated radiation efficiency, $\eta_R = 2\mu E_R / (\Delta\sigma_E M_0)$, is 0.58, and along with the pulse-like rupture, indicates a relatively energetic and brittle rupture process, although this is likely an upper bound given some underestimation in the static stress drop (Ye et al., 2013, 2016b).

3. Global analysis of aftershock productivity

Occurrence of only one early M4.4 aftershock near the rupture of the 2019 earthquake (Fig. 1b) may provide insight into the faulting in this region. The relatively brittle rupture process of the mainshock rules out the speculation that a dissipative mainshock rupture process inhibited aftershock nucleation. To provide a context for aftershock productivity of large intermediate-depth earthquakes, we examine global occurrences to evaluate any regional patterns associated with the tectonic setting or thermal factors.

We measure the number of aftershocks with magnitude ≥ 4.5 within 45 days following all major earthquakes with magnitude

≥ 7.0 since 1976 using the USGS-NEIC catalog. Mainshocks are grouped into shallow (0-70 km), intermediate-depth (70-350 km) and deep-focus (350-700 km) events according to the centroid depth estimates from the gCMT catalog. We exclude large events in the aftershock sequence of a larger mainshock, but include M7+ events followed by a nearby larger event ($\sim 5\%$ for all M7 events). With these criteria, we have 408 shallow, 90 intermediate-depth and 49 deep mainshocks (Fig. 5a). Aftershock search area is specified by a circle with radius R (in km) equal to twice the empirical rupture length from Wells and Coppersmith (1994), i.e., $R = 2 \times 10^{-2.44+0.59M_W}$, with M_W from the gCMT catalog. We constrain aftershock depths to be within ± 50 km of intermediate-depth and deep-focus mainshocks, and within ± 30 km for shallow mainshocks. Choices of aftershock space-time windows are subjective, but relative productivity measures are not particularly sensitive to windowing (Dascher-Cousineau et al., 2020). Fig. 5a shows

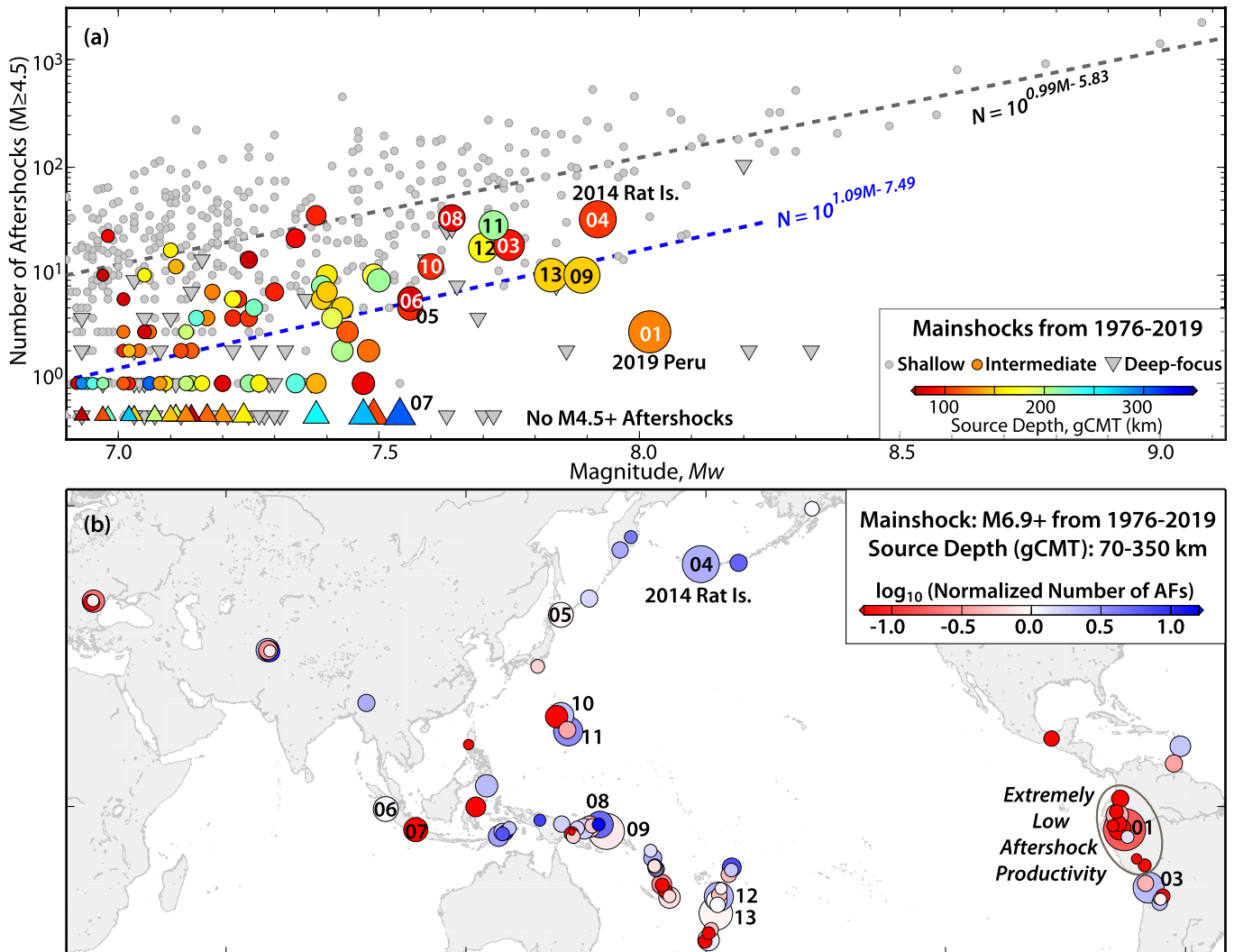


Fig. 5. (a) Number of M4.5+ aftershocks within 45 days for large mainshocks ($M_w > 6.9$) from 1976–2019 using the USGS-NEIC catalog. Note the very low value for the 2019 Peru earthquake relative to other intermediate-depth events with comparable size. Intermediate-depth (color triangles) and deep-focus (gray inverse triangles) earthquakes without M4.5+ aftershocks are plotted at $N = 0.5$. (b) Map view of the relative aftershock productivity normalized by the blue regression in (a) for large intermediate-depth earthquakes from 1976–2019. Note the regional low aftershock productivity for intermediate-depth earthquakes beneath Ecuador–Peru–Bolivia. Numbers of 01 to 13 in both (a) and (b) indicate large to great intermediate-depth earthquakes with detailed displays of background seismicity and aftershock sequences in Figs. 7–10 and S11–23.

the number of M4.5+ aftershocks for our space-time windows, plotted against mainshock magnitude.

Following the general aftershock productivity law, e.g., Reasenberg–Jones Law (Reasenberg and Jones, 1989), we perform a linear regression between the median value of number of aftershocks in every 0.1 magnitude bin, N , and mainshock magnitude M_w in log-linear space. For shallow events and our windowing choices, aftershock productivity varies with mainshock magnitude as $N = 10^{0.99M_w - 5.83}$. This is compatible with the estimates for varying space-time windows for all global activity found by Dascher-Cousineau et al. (2020). For the intermediate-depth earthquakes, a large number (22) of M7.0–7.5 mainshocks do not have any detected M4.5+ aftershocks, and the general trend based on the median values (including zero values) is $N = 10^{1.09M_w - 7.49}$. The order of magnitude lower productivity for intermediate-depth activity is consistent with the depth-dependence found by Dascher-Cousineau et al. (2020). For deep-focus earthquakes (inverted gray triangles in Fig. 5a), 17 mainshocks do not have M4.5+ aftershocks and many others have very few aftershocks; as a result, our sampling is too small to provide a stable regression. The low aftershock productivity for many large deep-focus earthquakes could be due to having a distinct nucleation mechanism from shallow and

intermediate-depth earthquakes. While intermediate-depth earthquakes have on average an order of magnitude lower aftershock productivity relative to the shallow events, the similar magnitude-scaling slopes of ~ 0.99 – 1.09 suggest that the faulting process may be similar. However, the 2019 Peru earthquake stands out among the intermediate-depth events as having markedly low aftershock productivity (Fig. 5a).

We map the relative aftershock productivity of the 90 intermediate-depth mainshocks as deviations from the magnitude-dependent trend (Fig. 5b). The low productivity of the 2019 Peru event is shared by most intermediate-depth earthquakes beneath Ecuador, Peru, and Bolivia. Other regions are either consistently high productivity (Aleutian, Kurils, Solomon Islands), or variable aftershock productivity (Chile, Tonga, Vanuatu, Indonesia). This suggests the low aftershock productivity may be associated with the tectonic setting of the Peru slab.

3.1. Thermal effect

Aftershock productivity for deep-focus earthquakes has systematic variation with slab thermal structure, i.e. more aftershocks for deep events in cold slabs (e.g., Wiens and Gilbert, 1996). To first

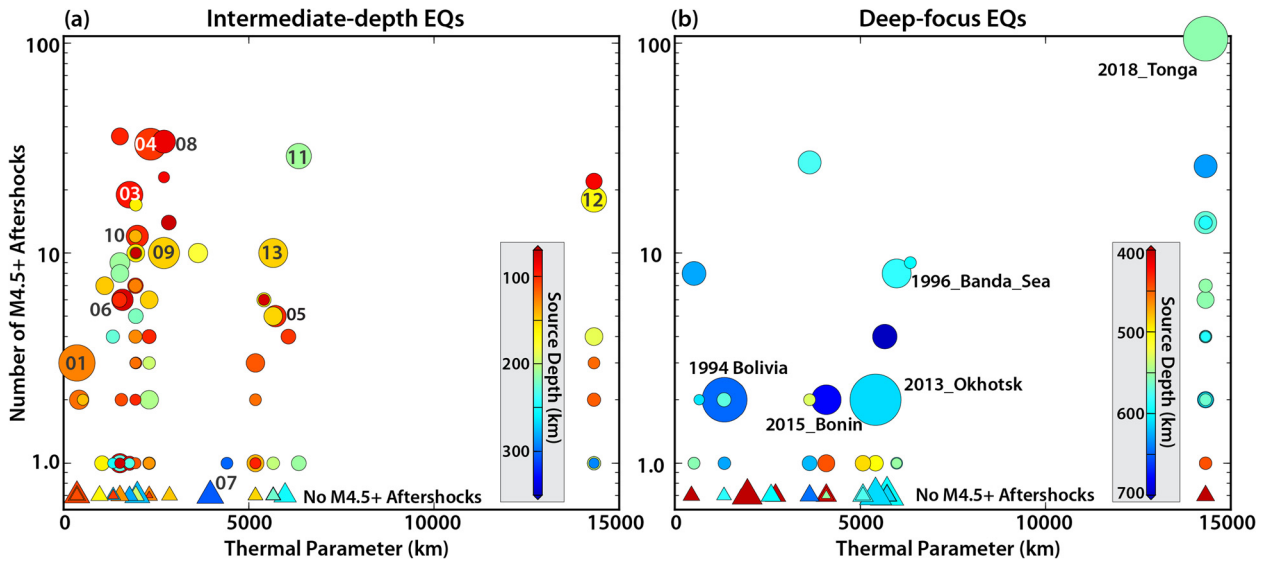


Fig. 6. Variation of number of aftershocks (magnitude ≥ 4.5) with slab thermal parameter for intermediate-depth earthquakes (left) and deep-focus earthquakes (right). Symbol color indicates source depth. Symbol sizes are scaled with M_w . Correction for magnitude dependent scaling using the intermediate-depth event regression shown in Fig. 5a gives results shown in Fig. S8.

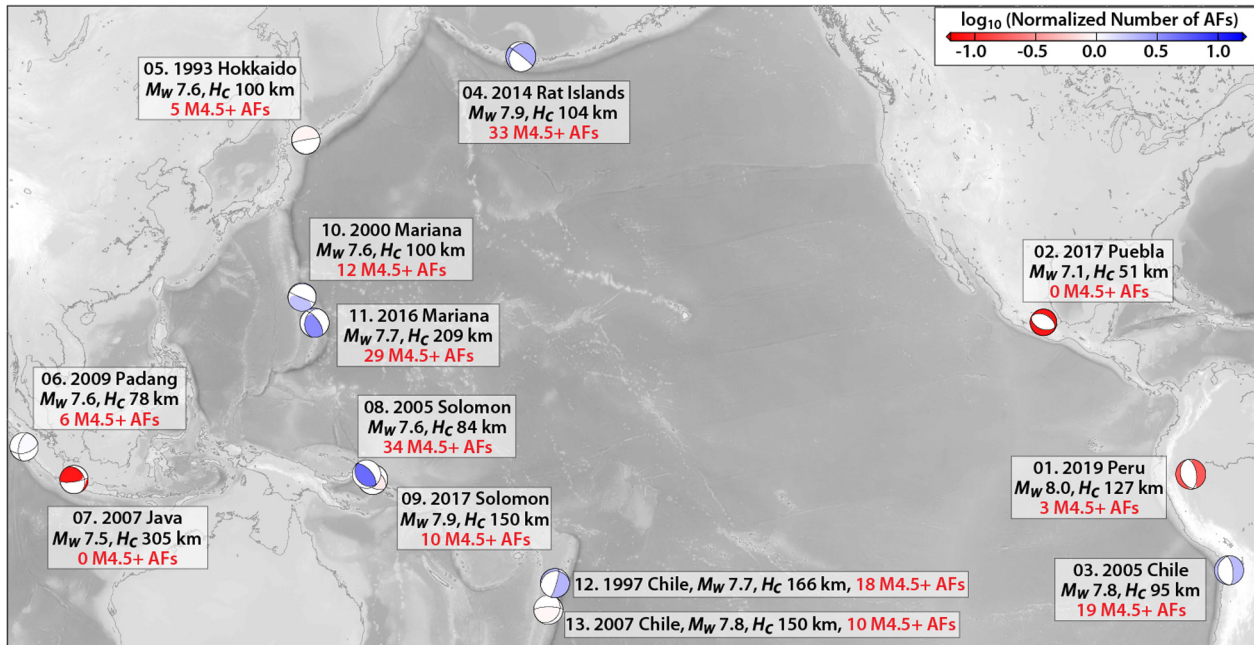


Fig. 7. Map of 13 large intermediate-depth earthquakes of interest. gCMT focal mechanisms are colored by centroid source depths. Nearby gCMT focal mechanisms from 1976 to 2019 and aftershock sequences for each event are shown in Figs. 8–10 and S11–S23.

order, slab temperature is usually characterized by the thermal parameter, calculated from age of the incoming plate at the trench multiplied by convergence velocity and sine of slab dip. It is essentially a measure of thickness of the incoming plate thermal boundary layer projected down into surrounding mantle heating conditions that thin the boundary layer with time similarly in different regions. Thus, the thermal parameter gives guidance on relative thickness of low temperature slab core projected along the average convergence path, which controls the time over which surrounding mantle heats the slab. Here we adopt thermal parameters for global subduction zones estimated by Syracuse et al. (2010) and investigate any correlation with aftershock productivity for large intermediate-depth and large deep-focus earthquakes from 1976 to 2019.

There are not strong overall correlations between aftershock productivity for the 90 large intermediate-depth earthquakes and slab thermal parameter (Figs. 6a and S8a), plate age (Fig. S9a) or convergence rate (Fig. S10a). However, the 2019 Peru event, along with other events in the same region, has a very low thermal parameter, partly due to the low slab dip. The flat slab environment inhibits thinning of the thermal boundary layer compared to more steeply dipping slabs.

For the 49 large deep-focus earthquakes in our dataset, there is a weak positive trend between thermal parameter and number of M4.5+ aftershocks (Fig. 6b) and a stronger trend with magnitude-scaled aftershock productivity (Fig. S8b). There are relatively more aftershocks in the high thermal parameter Tonga slab, and fewer aftershocks in the low thermal parameter South American slab. The overall pattern for deep-focus earthquakes found here us-

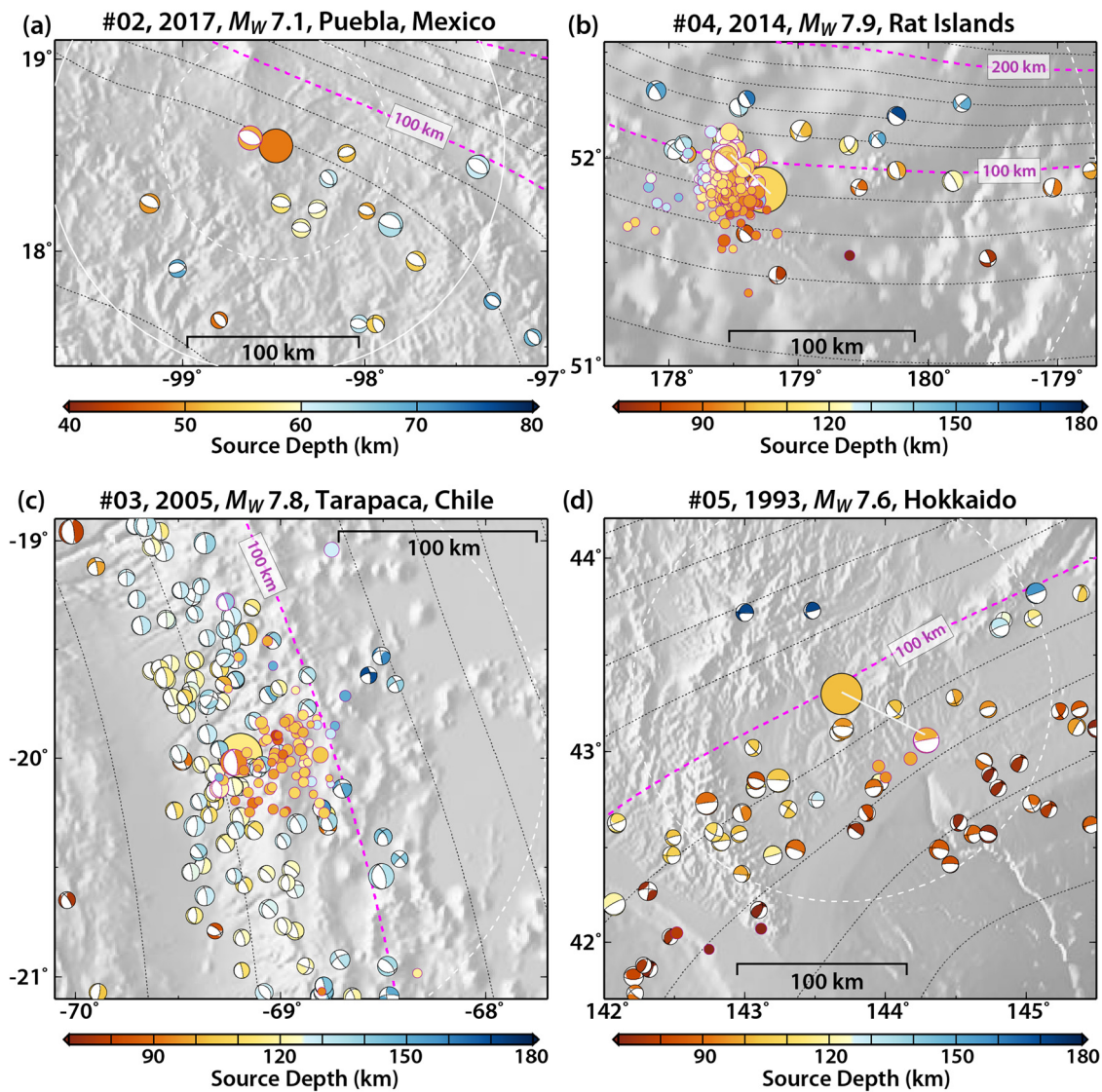


Fig. 8. Background earthquake focal mechanisms and 45-day aftershocks for (a) 2017 M_W 7.1 Puebla-Morelo, Mexico earthquake, (b) 2014 M_W 7.9 Rat Islands earthquake, (c) 2005 M_W 7.8 Tarapaca, Chile earthquake, and (d) 1993 M_W 7.6 Hokkaido, Japan earthquake. Focal mechanisms from the gCMT catalog for intermediate-depth earthquakes from 1976 to 2019. Aftershocks within 45 days in the USGS-NEIC catalog (circles) are shown, along with their available gCMT focal mechanisms with best-double-couple plotted with magenta lines. The black dashed curves are 20 km depth contours of the slab interface from Slab2 (Hayes et al., 2018), with 100 km depth contour highlighted in magenta. The dashed white circle has a radius R from the USGS-NEIC epicenter of the mainshock equal to the empirical rupture length from Wells and Coppersmith (1994). The solid white circle has radius $2R$ and is used for the aftershock search window. Corresponding aftershock sequences plotted versus time are shown in Figs. S12-S15.

ing updated thermal parameters from Syracuse et al. (2010) and more earthquakes sampling, is less pronounced than that found by Wiens and Gilbert (1996).

It does not appear that temperature is the dominant control on aftershock productivity variation across the full population of large intermediate-depth earthquakes. Possibly, the current spatial sampling of thermal parameter is too sparse to reveal a robust correlation with aftershock productivity for characteristic lengths less than 100 km.

3.2. Regional structural and stress heterogeneity

Based on comparison with microfracture experiments, the frequency-magnitude relation and characteristics of the foreshock-aftershock sequence of earthquakes have been related to the degree of structural heterogeneity and the uniformity of the regional applied stress (e.g., Mogi, 1962a, 1962b, 1963; Scholz, 1968). In contrast to interplate ruptures for large shallow earthquakes on subduction megathrusts or major strike-slip faults, where after-

shocks tend to occur on or close to the same fault plane with the mainshock, foreshock-mainshock-aftershock sequences at intermediate depth may be more likely to occur in a more distributed volume, similar to the microfracture experiments by Mogi. The spatial distribution and stress orientations for all large intermediate-depth earthquakes for the last 40 years beneath Peru (Figs. 1 and S11) suggest that the 3D seismogenic structures are relatively homogeneous and the applied stress for earthquake nucleation is relatively uniform, facilitated by the near-horizontal slab environment with a uniform extensional stress regime (Sandiford et al., 2019).

To evaluate the regional structural and stress heterogeneity more broadly, we consider aftershock sequences with $M \geq 4.5$ events for the 12 largest ($M_W \geq 7.5$) intermediate-depth earthquakes from 1976 to 2019, along with the 2017 M_W 7.1 Puebla-Morelos, Mexico earthquake (Fig. 7). The total absence of aftershocks is notable for the latter 2017 Puebla-Morelos, Mexico intraslab normal-faulting earthquake, located near the eastern end of a flat slab (Figs. 8a and S12) in a similar configuration to that for the 2019 Peru earthquake. Whereas for the high aftershock pro-

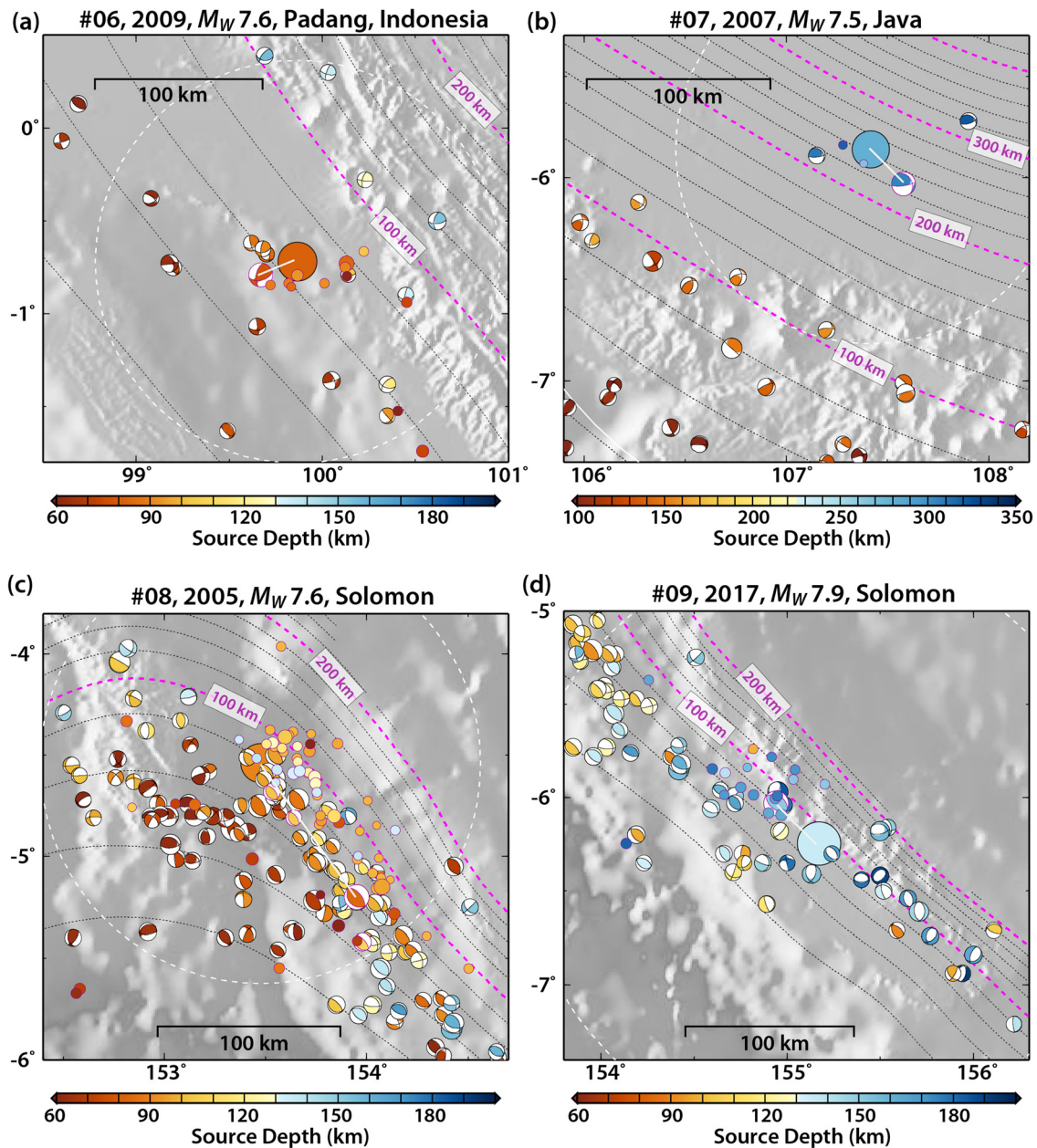


Fig. 9. Background earthquake focal mechanisms and 45-day aftershocks for (a) 2009 M_W 7.6 Padang, Indonesia earthquake, (b) 2007 M_W 7.5 Java, Indonesia earthquake, (c) 2005 M_W 7.6 Solomon earthquake, and (d) 2017 M_W 7.9 Solomon earthquake. Other symbols are same as Fig. 8. Corresponding aftershock sequences plotted versus time are shown in Figs. S16-S19.

ductivity 2014 Rat Island earthquake (M_W 7.9, depth \sim 104 km), the second largest intermediate-depth earthquake with modern broadband seismological recordings, the background seismicity and earthquake focal mechanisms are more variable (Figs. 8b and S14). This may be due to heterogeneous structure and stress distribution resulting from a complex 3D slab geometry (e.g., Twardzik and Ji, 2015).

The 2005 Tarapaca, Chile earthquake (M_W 7.8, \sim 95 km) has relatively similar regional focal mechanisms, but much higher background rate and aftershock productivity than the 2019 Peru event (Figs. 8c and S13). This activity is below the Andes in a region of gradually increasing slab dip, in contrast to flat Peruvian slab, but with similar lithospheric age and convergence rate to that along Peru. Deformation of the slab beneath the Andean keel near the curvature along the coast from Northern Chile to Southern Peru and the down-dip curvature may account for the higher background

rates and higher aftershock productivity relative to the Peru environment.

The 1993 Hokkaido, Japan earthquake (M_W 7.6, \sim 100 km) with relatively high aftershock productivity is located at the junction between the Kuril and northern Honshu subduction zones, where the slab is strongly distorted, as indicated by the variable background focal mechanisms (Figs. 7, 8d and S15). More small aftershocks were detected by the local Japanese seismic network. Ozel and Moriya (1999) found strong variation in focal mechanisms and attributed it to the highly inhomogeneous stress state in the source region.

The other large intermediate-depth earthquakes with high aftershock productivity, such as the 2005 Solomon (M_W 7.6, \sim 90 km; Figs. 9c and S18), 2017 Solomon (M_W 7.9, \sim 150 km; Figs. 9d and S19), 2000 Marianas (M_W 7.7, \sim 209 km; Figs. 10a and S20), and 2016 Marianas (M_W 7.6, \sim 100 km; Figs. 10b and S21) earthquakes are also located within regionally distorted slabs, with in-

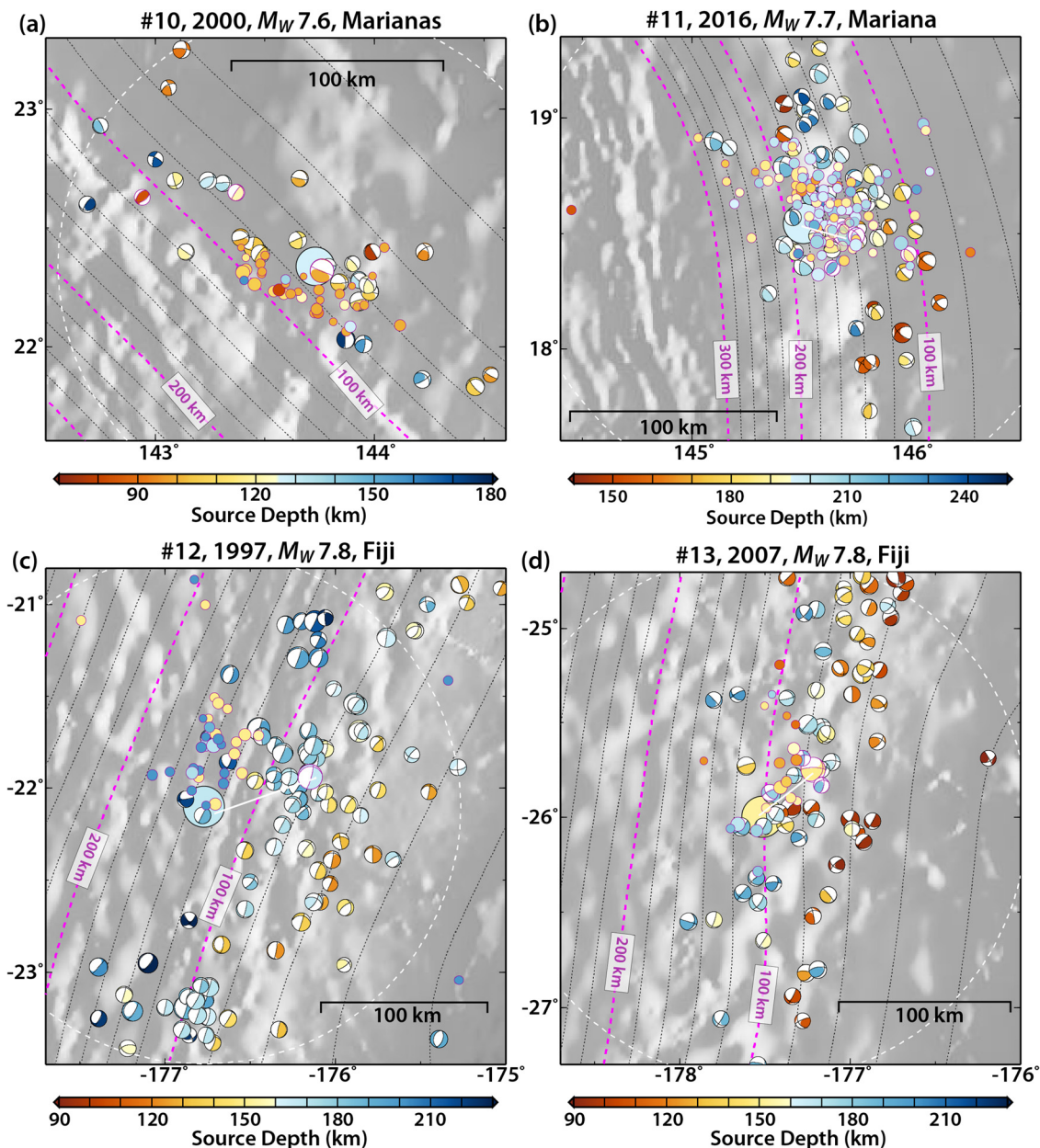


Fig. 10. Background earthquake focal mechanisms and 45-day aftershocks for (a) 2000 M_W 7.6 Marianas earthquake, (b) 2016 M_W 7.7 Mariana earthquake, (c) 1997 M_W 7.8 Fiji earthquake, and (d) 2007 M_W 7.8 Fiji earthquake. Other symbols are same as Fig. 8. Corresponding aftershock sequences plotted versus time are shown in Figs. S20–S23.

homogeneous stress state indicated by the variety in earthquake focal mechanisms.

The 2009 Padang, Indonesia earthquake (M_W 7.6, ~ 78 km; Figs. 9a and S16) with moderate aftershock productivity is located at a relatively shallow depth in the Sumatra slab compared to other large intermediate-depth events (Fig. 7). The oblique focal mechanism of the mainshock and background earthquakes reveals a complex slab stress state at intermediate depth, but the faulting is relatively uniform near the large M_W 7.6 event.

Tonga has a very steeply dipping slab with a high level of continuously-distributed intermediate and deep focus activity that contrasts strongly with Peru. While there are portions of the slab that have uniform mechanisms, there is much more along-strike variability than observed in the flat Peru slab. For the 2007 Fiji intermediate-depth earthquake (M_W 7.8, ~ 150 km), the focal mechanisms of both background activity and aftershocks are quite variable locally (Figs. 10d and S23), while for the 1997 Fiji event (M_W 7.7, ~ 165 km) the mechanisms are less variable (Figs. 10c,

S22). The change in complexity between these large Tonga mainshocks over a fairly short separation distance emphasizes the along-strike variability in deformation associated with contortion of the Tonga slab, as studied by many investigators. We view the higher aftershock productivity of the Tonga events as also being a manifestation of the more complex stress state in the Tonga slab. In contrast, Figs. 1a and S11 show that the nearly-horizontal Peru slab has sparser and more uniform faulting, indicative of a more uniform stress regime over a large region along-strike in the Peruvian slab.

There are only two M4.1 and M3.9 aftershocks for the 2007 Java, Indonesia earthquake (M_W 7.5, ~ 305 km; Figs. 9b and S17). This is the deepest among all large intermediate-depth earthquakes with $M_W \geq 7.5$ since 1976 (Fig. 7). The intermediate-depth seismicity within the slab in western Java is relatively low, and the aseismic separation from a lineation of deep-focus seismicity at 600–700 km resembles that within the slab from Colombia to Peru. The 2007 Java earthquake is located at the northeastern edge

of the intermediate-depth seismicity (Figs. 9b and S17), similar to the situation for the 2019 Peru event. The background seismicity around this large magnitude 7.5 event is also low, and two M_W 5.2 events in 1993 and 1994 have similar focal mechanisms to that for the M_W 7.5 mainshock (Fig. 9b), suggesting a relatively uniform downdip extensional stress state around the source area. The precision of the slab model geometry in this region is relatively low due to the sparse seismicity, but the M_W 7.5 mainshock does not appear to be in a flattened slab or near a steeply plunging edge of the slab.

Melgar et al. (2018) assert that the proximity to abrupt steepening of the Mexico slab, in combination with influence of pre-existing faulting, accounts for the 2017 Puebla-Morelos event. For the 2019 Peru earthquake, the position of the slab is somewhat unclear, but if we adjust the Slab 1.0 or Slab 2.0 models to account for the location of the 2019 event, it is likely near the steepening region. But the faulting geometry and lack of aftershocks indicate that the Peru event behaves similarly to large events to the west in the flat Peru slab, far from the bend, so it appears that the role of the slab-pull is similar in terms of faulting that is activated. While the slab geometry is not precisely known, the 2019 event is not in the steepest slab curvature region; indeed, for both the Peru and Puebla-Morelos regions that the strongest slab bending is aseismic. The relative uniformity of faulting indicates relative uniformity of stress in low curvature slabs, compared to regions with continuous curvature and along-strike variability. This is generally consistent with numerical modeling by Sandiford et al. (2019) if we focus on the seismogenic portions of the flat slabs under Mexico and Peru. Thus, we find it reasonable to infer that the markedly low aftershock productivity for the 2019 M_W 8.0 Peru earthquake is likely due to relative homogeneity of seismogenic structure (inherited faults caused by bending and unbending in the up-dip part of the slab) with uniformity of applied stress in the flat-lying portion of the Nazca slab beneath Peru.

4. Conclusions

The 2019 Peru earthquake occurred near the eastern end of the flat slab beneath Peru in a region with little prior activity. The minor non-double-couple moment tensor component and similar focal mechanism to the regional seismicity suggest relatively uniform strain regime in the slab environment. The source process resolved from back-projection imaging and finite-fault modeling shows unilaterally northward rupture expansion with three distinct patches of up to ~ 4.5 m slip along a rupture zone extending ~ 170 km. Low static stress drop and high radiation efficiency indicate a brittle, energetic faulting. The aftershock productivity was markedly low for an M_W 8.0 event, even among globally low productivity intermediate-depth events. The systematically low aftershock productivity for intermediate-depth earthquakes beneath Peru appears to be associated with the homogeneity in faulting and stress state in the nearly horizontal slab.

CRedit authorship contribution statement

LY performed back-projection analysis and finite-fault inversion; HK conducted W -phase inversion; LY and TL designed aftershock productivity analysis; LY, TL and HK conceived the project, interpreted the result and wrote the manuscript collaboratively.

Declaration of competing interest

The authors declare that they have no known competing financial interests or personal relationships that could have appeared to influence the work reported in this paper.

Acknowledgements

Teleseismic body wave waveforms were downloaded from the Incorporated Research Institutions for Seismology (IRIS) data management center (http://ds.iris.edu/wilber3/find_event). Global Centroid Moment Tensor Solutions are from <https://www.globalcmt.org/CMTsearch.html>. Aftershock analysis is based on the earthquake catalog from National Earthquake Information Center at U.S. Geological Survey (USGS-NEIC) (<https://earthquake.usgs.gov/earthquakes/>), last accessed in November 11, 2019. We thank Dr. Dan Sandiford, an anomalous reviewer and the editor Rebecca Bendick for their constructive review. K.D. Koper kindly provided his back-projection software. Lingling Ye's earthquake study is supported by National Natural Science Foundation of China (No. 41874056) and Fundamental Research Funds for the Central Universities, Sun Yat-sen University (No. 19lgzd11). Thorne Lay's earthquake research is supported by The National Science Foundation (Grant EAR1802364).

Appendix A. Supplementary material

Supplementary material related to this article can be found online at <https://doi.org/10.1016/j.epsl.2020.116528>.

References

- Adams, M., Hao, J., Ji, C., 2019. Energy-based average stress drop and its uncertainty during the 2015 M_W 7.8 Nepal earthquake constrained by geodetic data and its implications to earthquake dynamics. *Geophys. J. Int.* 217, 2. <https://doi.org/10.1093/gji/ggz047>.
- Astiz, L., Lay, T., Kanamori, H., 1988. Large intermediate-depth earthquakes and the subduction process. *Phys. Earth Planet. Inter.* 53, 80–166.
- Campus, P., Das, S., 2000. Comparison of the rupture and radiation characteristics of intermediate and deep earthquakes. *J. Geophys. Res., Solid Earth* 105 (B3), 6177–6189.
- Dascher-Cousineau, K., Brodsky, E.E., Lay, T., Goebel, T.H.W., 2020. What controls variations in aftershock productivity? *J. Geophys. Res., Solid Earth* 125, e2019JB01811.
- Delouis, B., Legrand, D., 2007. M_W 7.8 Tarapaca intermediate depth earthquake of 13 June 2005 (northern Chile): fault plane identification and slip distribution by waveform inversion. *Geophys. Res. Lett.* 34, L01304. <https://doi.org/10.1029/2006GL028193>.
- Dziewonski, A.M., Anderson, D.L., 1981. Preliminary reference Earth model. *Phys. Earth Planet. Inter.* 25 (4), 297–356.
- Ekström, G., Nettles, M., Dziewonski, A.M., 2012. The global CMT project 2004–2010: centroid-moment tensors for 13,017 earthquakes. *Phys. Earth Planet. Inter.* 200–201 (1–9), 2012. <https://doi.org/10.1016/j.pepi.2012.04.002>.
- Emry, E.L., Wiens, D.A., Garcia-Castellanos, D., 2014. Faulting with the Pacific Plate at the Mariana Trench: implications for plate interface coupling and subduction of hydrous minerals. *J. Geophys. Res., Solid Earth* 119, 3076–3095.
- Faccenda, M., Gerya, T.V., Burlini, L., 2009. Deep slab hydration induced by bending-related variations in tectonic pressure. *Nat. Geosci.* 2, 790–793.
- Green, H.W., Houston, H., 1995. The mechanics of deep earthquakes. *Annu. Rev. Earth Planet. Sci.* 23, 169–213.
- Hacker, B.R., Peacock, S.M., Abers, G.A., Holloway, S.D., 2003. Subduction factory 2: are intermediate-depth earthquakes in subducting slabs linked to metamorphic dehydration reactions? *J. Geophys. Res., Solid Earth* 108 (B1), 2030.
- Hartzell, S.H., Heaton, T.H., 1983. Inversion of strong ground motion and teleseismic waveform data for the fault rupture history of the 1979 Imperial Valley, California, earthquake. *Bull. Seismol. Soc. Am.* 73 (6A), 1553–1583.
- Hayes, G.P., Moore, G.L., Portner, D.E., Hearne, M., Flamme, H., Furtney, M., Smoczyk, G.M., 2018. Slab2, a comprehensive subduction zone geometry model. *Science* 362 (6410), 58–61.
- Hobbs, B.E., Ord, A., 1988. Plastic instabilities: implications for the origin of intermediate and deep focus earthquakes. *J. Geophys. Res., Solid Earth* 93, 10,521–10,540.
- Houston, H., Benz, H.M., Vidale, J.E., 1998. Time functions of deep earthquakes from broadband and short-period stacks. *J. Geophys. Res., Solid Earth* 103, 29,895–29,913.
- John, T., Medvedev, S., Rupke, L.H., Andersen, T.B., Podladchikov, Y.Y., Aussreheim, H., 2009. Generation of intermediate-depth earthquakes by self localizing thermal runaway. *Nat. Geosci.* 2, 137–140.
- Jung, H., Green, H.W., Dobrzynetska, L.F., 2004. Intermediate-depth earthquake faulting by dehydration embrittlement with negative volume change. *Nature* 428, 545–549.

- Kanamori, H., Rivera, L., 2008. Source inversion of *W* phase: speeding up seismic tsunami warning. *Geophys. J. Int.* 175, 222–238.
- Kelemen, P.B., Hirth, G., 2007. A periodic shear-heating mechanism for intermediate-depth earthquakes in the mantle. *Nature* 446, 787–790.
- Kikuchi, M., Kanamori, H., 1991. Inversion of complex body waves—III. *Bull. Seismol. Soc. Am.* 81 (6), 2335–2350.
- Kirby, S., Engdahl, E.R., Denlinger, R., 1996. Intermediate-depth intraslab earthquakes and arc volcanism as physical expressions of crustal and uppermost mantle metamorphism in subducting slabs. *Geophys. Monogr.* 96, 195–214.
- Kuge, K., Kawakatsu, H., 1993. Significance of non-double couple components of deep and intermediate-depth earthquakes: implications from moment tensor inversions of long-period seismic waves. *Phys. Earth Planet. Inter.* 75 (4), 243–266.
- Laske, G., Masters, G., Ma, Z., Pasyanos, M., 2013. Update on CRUST1.0 – a 1-degree global model of Earth's crust. *Geophys. Res. Abstr.* 15. Abstract EGU2013-2658.
- Li, J., Zheng, Y., Thomsen, L., Lapen, T.J., Fang, X., 2018. Deep earthquakes in subducting slabs hosted in highly anisotropic rock fabric. *Nat. Geosci.* 11 (9), 696–700.
- Liu, W., Yao, H., 2020. Rupture process of the 26 May 2019 Mw 8.0 Northern Peru intermediate-depth earthquake and insights into its mechanism. *Geophys. Res. Lett.* 47, e2020GL087167.
- McCloskey, J., Lange, D., Tilmann, F., Nalbant, S.S., Bell, A.F., Natawidjaja, D.H., Rietbrok, A., 2010. The September 2009 Padang earthquake. *Nat. Geosci.* 3, 70–71.
- Melgar, D., Pérez-Campos, X., Ramírez-Guzmán, L., Spica, Z., Espíndola, V.H., Hammond, W.C., Cabral-Cano, E., 2018. Bend faulting at the edge of a flat slab: the 2017 M_W 7.1 Puebla-Morelos, Mexico earthquake. *Geophys. Res. Lett.* 45, 2633–2641.
- Meng, Q., Heeszel, D.S., Ye, L., Lay, T., Wiens, D.A., Jia, M., Cummins, P.R., 2015. The 3 May 2006 (Mw 8.0) and 19 March 2009 (Mw 7.6) Tonga earthquakes: intraslab compressional faulting below the megathrust. *J. Geophys. Res., Solid Earth* 120 (9), 6297–6316.
- Mogi, K., 1962a. Study of elastic shocks caused by the fracture of heterogeneous materials and its relation to earthquake phenomena. *Bull. Earthq. Res. Inst. Univ. Tokyo* 40, 125–173.
- Mogi, K., 1962b. Magnitude-frequency relation for elastic shocks accompanying fractures of various materials and some related problems in earthquakes. *Bull. Earthq. Res. Inst. Univ. Tokyo* 40, 831–853.
- Mogi, K., 1963. Some discussions on aftershocks, foreshocks and earthquake swarms—the fracture of a semi-infinite body caused by an inner stress origin and its relation to the earthquake phenomena. *Bull. Earthq. Res. Inst. Univ. Tokyo* 41, 615–658.
- Ogawa, M., 1987. Shear instability in a viscoelastic material as the cause of deep focus earthquakes. *J. Geophys. Res., Solid Earth* 92, 13801–13810.
- Okada, Y., 1985. Surface deformation due to shear and tensile faults in a half-space. *Bull. Seismol. Soc. Am.* 75 (4), 1135–1154.
- Okazaki, K., Hirth, G., 2016. Dehydration of lawsonite could directly trigger earthquakes in subducting oceanic crust. *Nature* 530, 81–84.
- Ozel, N., Moriya, T., 1999. Different stress directions in the aftershock focal mechanisms of the Koshiro-Oki earthquake of Jan. 15, 1993, SE Hokkaido, Japan, and horizontal rupture in the double seismic zone. *Tectonophysics* 313 (3), 307–327.
- Peacock, S., 2001. Are the lower planes of double seismic zones caused by serpentine dehydration in subducting oceanic mantle? *Geology* 29, 299–302.
- Prieto, G., et al., 2013. Seismic evidence for thermal runaway during intermediate-depth earthquake rupture. *Geophys. Res. Lett.* 40, 6064–6068.
- Raleigh, C.B., Paterson, M.S., 1965. Experimental deformation of serpentinite and its tectonic implications. *J. Geophys. Res., Solid Earth* 70, 3965–3985.
- Ranero, C.R., Villasenor, A., Morgan, J.P., Weinreber, W., 2005. Relationship between bend-faulting at trenches and intermediate-depth seismicity. *Geochem. Geophys. Geosyst.* 6, Q12002.
- Reasenber, P.A., Jones, L.M., 1989. Earthquake hazard after a mainshock in California. *Science* 243 (4895), 1173–1176.
- Sandiford, D., Moresi, L., Sandiford, M., Yang, T., 2019. Geometric controls on flat slab seismicity. *Earth Planet. Sci. Lett.* 527, 115787.
- Scholz, C.H., 1968. The frequency-magnitude relation of microfracturing in rock and its relation to earthquakes. *Bull. Seismol. Soc. Am.* 58 (1), 399–415.
- Shiina, T., Nakajima, J., Matsuzawa, T., Toyokuni, G., Kita, S., 2017. Depth variations in seismic velocity in the subducting crust: evidence for fluid-related embrittlement for intermediate-depth earthquakes. *Geophys. Res. Lett.* 44, 810–817.
- Syracuse, E.M., van Keken, P.E., Abers, G.A., 2010. The global range of subduction zone thermal models. *Phys. Earth Planet. Inter.* 183 (1–2), 73–90.
- Tibi, R., Bock, G., Estabrook, C.H., 2002. Seismic body wave constraint on mechanisms of intermediate-depth earthquakes. *J. Geophys. Res., Solid Earth* 107 (B3), 2047. <https://doi.org/10.1029/2001JB000361>.
- Twardzik, C., Ji, C., 2015. The Mw 7.9 2014 intraplate intermediate-depth Rat Islands earthquake and its relation to regional tectonics. *Earth Planet. Sci. Lett.* 431, 26–35.
- Wells, D.L., Coppersmith, K.J., 1994. New empirical relationships among magnitude, rupture length, rupture width, rupture area, and surface displacement. *Bull. Seismol. Soc. Am.* 84 (4), 974–1002.
- Wiemer, S., Benoit, J.P., 1996. Mapping the *b*-value anomaly at 100 km depth in the Alsea and New Zealand subduction zones. *Geophys. Res. Lett.* 23, 1557–1560.
- Wiens, D.A., Gilbert, H.J., 1996. Effect of slab temperature on deep-earthquake aftershock productivity and magnitude-frequency relations. *Nature* 384, 153–156.
- Wiens, D.A., Gilbert, H.J., Hicks, B., Wyssession, M.E., Shore, P.J., 1997. Aftershock sequences of moderate-sized intermediate and deep earthquakes in the Tonga subduction zone. *Geophys. Res. Lett.* 24 (16), 2059–2062.
- Xu, Y., Koper, K.D., Sufri, O., Zhu, L., Hutko, A.R., 2009. Rupture imaging of the Mw 7.9 12 May 2008 Wenchuan earthquake from back projection of teleseismic P waves. *Geochem. Geophys. Geosyst.* 10, Q04006.
- Ye, L., Lay, T., Bai, Y., Cheung, K.F., Kanamori, H., 2017. The 2017 M_W 8.2 Chiapas, Mexico, earthquake: energetic slab detachment. *Geophys. Res. Lett.* 44, 11,824–11,832.
- Ye, L., Lay, T., Kanamori, H., Koper, K.D., 2013. Energy release of the 2013 Mw 8.3 Sea of Okhotsk earthquake and deep slab stress heterogeneity. *Science* 341 (6152), 1380–1384.
- Ye, L., Lay, T., Kanamori, H., 2014. The 23 June 2014 M_W 7.9 Rat Islands archipelago, Alaska, intermediate depth earthquake. *Geophys. Res. Lett.* 41, 6389–6395.
- Ye, L., Lay, T., Kanamori, H., Rivera, L., 2016a. Rupture characteristics of major and great ($M_W \geq 7.0$) megathrust earthquakes from 1990–2015: 1. Source parameter scaling relationships. *J. Geophys. Res., Solid Earth* 121, 826–844.
- Ye, L., Lay, T., Kanamori, H., Zhan, Z., Duputel, Z., 2016b. Diverse rupture processes in the 2015 Peru deep earthquake doublet. *Sci. Adv.* 2 (6), e1600581.

1
2
3
4
5
6
7
8
9
10
11
12
13
14
15
16
17
18
19
20

Earth and Planetary Science Letters

Supporting Information for

**Anomalously Low Aftershock Productivity of the 2019 M_W 8.0
Energetic Intermediate-Depth Faulting beneath Peru**

Lingling Ye¹, Thorne Lay², Hiroo Kanamori³

¹ *Guangdong Provincial Key Lab of Geodynamics and Geohazards, School of Earth Sciences and Engineering, Sun Yat-sen University, Guangzhou, China.*

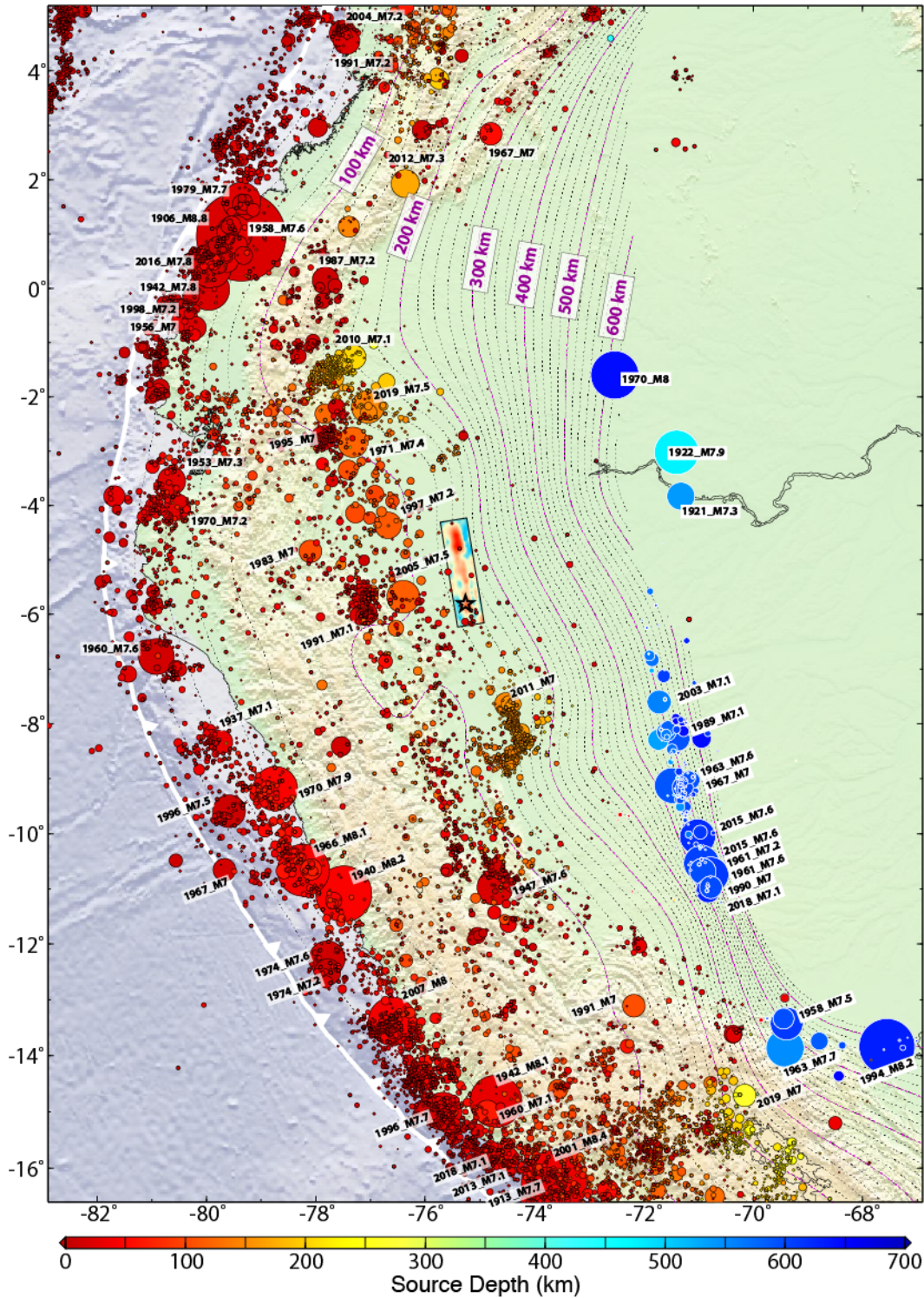
² *Department of Earth and Planetary Sciences, University of California Santa Cruz, Santa Cruz, California 95064, USA.*

³ *Seismological Laboratory, California Institute of Technology, Pasadena, California 91125, USA.*

Corresponding author: Lingling Ye (yelingling@mail.sysu.edu.cn)

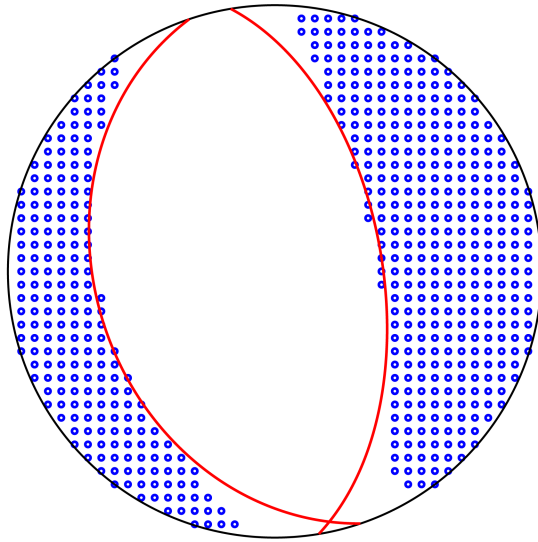
Introduction

This supporting information provides 23 additional figures to support the discussion in the main text.



21
22
23
24
25
26

Figure S1. Seismicity under northern Peru, Ecuador and western Brazil since 1900 from the USGS-NEIC catalog, color-coded for source depth. The radius of each circle is proportional to the event magnitude. The magenta- and black-dashed curves are 20 km depth contours of the slab interface from model Slab2 (Hayes et al., 2018). The star and rectangle area show the epicenter and slip distribution for the 2019 Peru earthquake (see details in Figure 1). Year and magnitude of events with $M \geq 7$ are labeled.



Moment Tensor [N-m x1e21]: -1.1621 -0.0814 1.2435 0.0434 -0.5471 -0.3470

Scalar moment [N-m]: 1.36e21 ($M_w = 8.02$)

Best Nodal planes (strike/dip/rake): 161.3/ 33.4/ -97.7 350.5/ 56.9/ -85.0

Eigenvalues [N-m x1e21]: 1.4417 -0.1603 -1.2815

Centroid: Lon -75.163°, Lat -5.407°, depth 140.5 km, Time shift T_c 36.0s

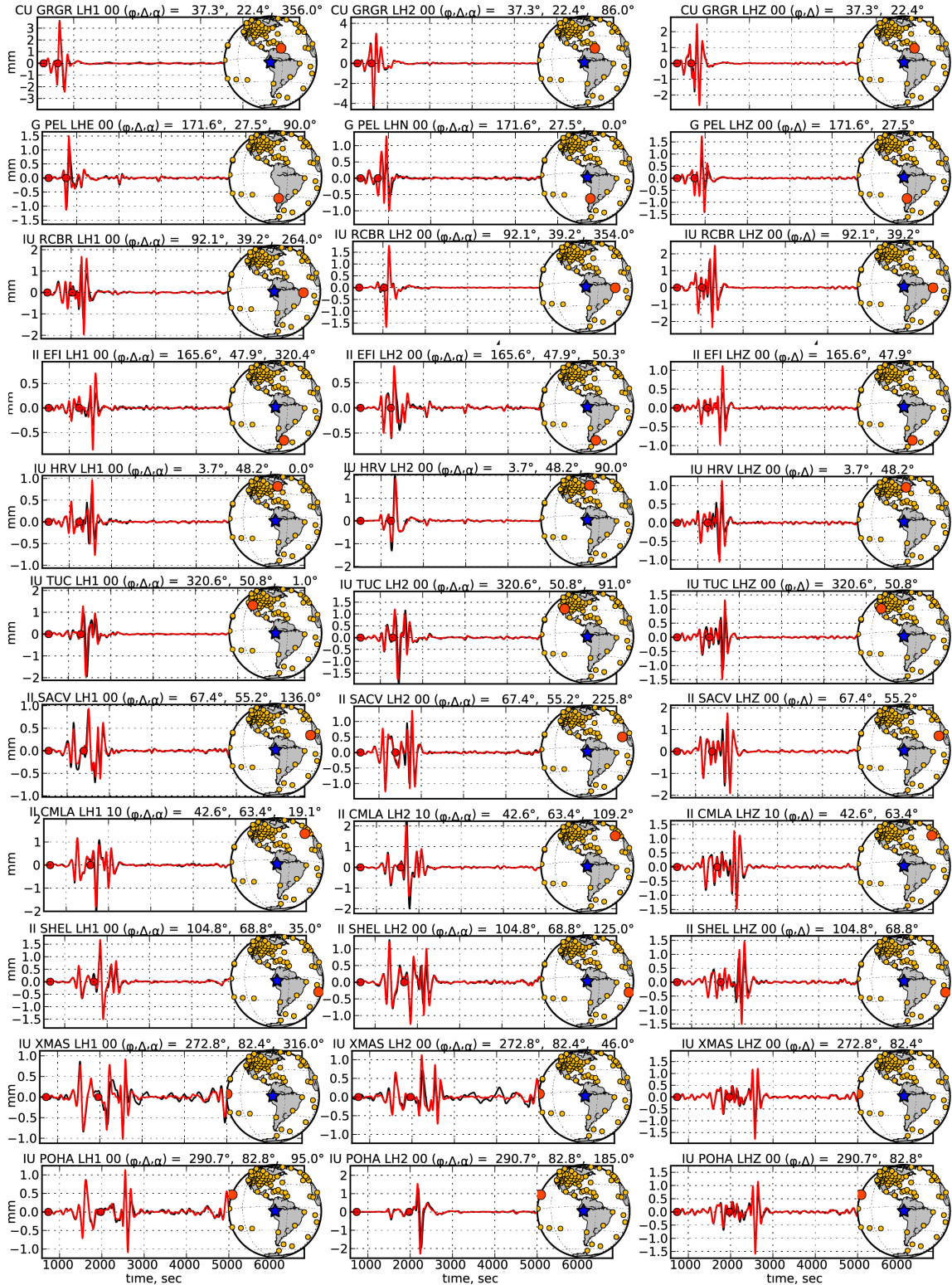
Filter parameters: 100 s - 600 s, 4th order, 1-pass butterworth filter

Used stations (80, 186 channels) :

GRGR(LH1,LH2,LHZ) TGUH(LH1,LH2,LHZ) MTDJ(LH1) BBGH(LH1,LH2) SDDR(LH2) SJG(LH2) GTBY(LH1) ANWB(LH2) GRTK(LH2)
 PEL(LHE,LHN,LHZ) SPB(LHE,LHN,LHZ) DWPF(LH1,LHZ) UNM(LHE,LHN,LHZ) BRAL(LH2,LHZ) RPN(LHZ) RCBR(LH1,LH2,LHZ)
 BBSR(LH1,LH2) KVTX(LHZ,LHZ) GOGA(LH1,LH2) HKT(LH1,LH2,LHZ) JCT(LH2,LHZ) BLA(LH2) WVT(LH1,LH2) MIAR(LH2,LHZ)
 WCI(LH2,LHZ) WMOK(LHZ) CCM(LH2,LHZ) SSPA(LH1) EFI(LH1,LH2,LHZ) HRV(LH1,LH2,LHZ) AAM(LH2) KSU1(LH1,LH2)
 ANMO(LH1,LH2,LHZ) JFWS(LH2) TUC(LH1,LH2,LHZ) MVCO(LH1,LH2,LHZ) ECSD(LH1,LH2) WUAZ(LH2,LHZ,LH1) ISCO(LH2,LH1,LHZ)
 SACV(LH1,LH2,LHZ) PFO(LH1,LH2,LHZ) EYMN(LH2) PTCN(LH2,LHZ) RSSD(LH1,LH2,LHZ) PASC(LHE,LHN) DUG(LH1,LH2,LHZ)
 HOPE(LH1,LHZ) PMSA(LH1,LHZ) DGMT(LH2,LHZ) SAO(LHN,LHZ) CMB(LHE,LHN,LHZ) ASCN(LH1,LH2,LHZ) HLID(LH2,LH1,LHZ)
 MBO(LHE,LHZ) EGMT(LHZ) WVOR(LH1,LH2,LHZ) MCCM(LHE,LHN,LHZ) CMLA(LH1,LH2,LHZ) FFC(LH2,LHZ) TRIS(LH1,LH2,LHZ)
 HAWA(LH1,LH2,LHZ) NEW(LH1,LH2,LHZ) COR(LH1,LH2,LHZ) NLWA(LH1,LH2,LHZ) SHEL(LH1,LH2,LHZ) SFJD(LH1,LH2)
 WRAK(LH1,LH2,LHZ) PAB(LH1,LH2,LHZ) BORG(LH1,LH2,LHZ) XMAS(LH1,LH2,LHZ) RAR(LH1) POHA(LH1,LH2,LHZ) TAM(LHE,LHZ)
 ESK(LH1,LH2,LHZ) KIP(LH1,LH2,LHZ) SSB(LHE,LHN,LHZ) COLA(LH1,LH2,LHZ) KDAK(LH1,LH2,LHZ) HGN(LHE,LHZ) ECH(LHE,LHN,LHZ)

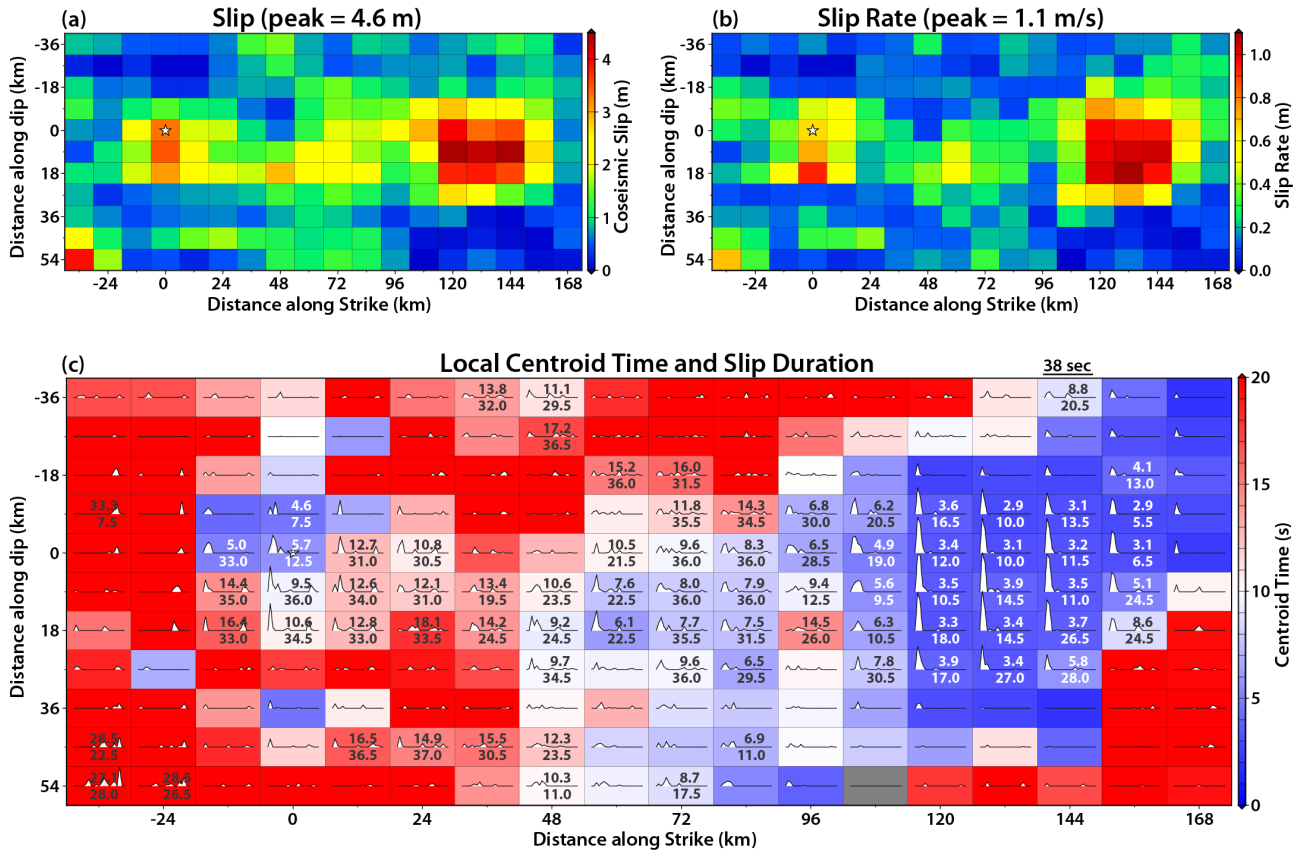
27
28

29 **Figure S2.** Moment-tensor inversion using W -phase waveforms in the passband 100 - 600 s. The inversion
 30 used waveforms from 80 stations and a total of 186 channels. The nodal planes for the best-double-couple are
 31 shown in red. A subset of the 186 waveform fits is shown in Figure S3.



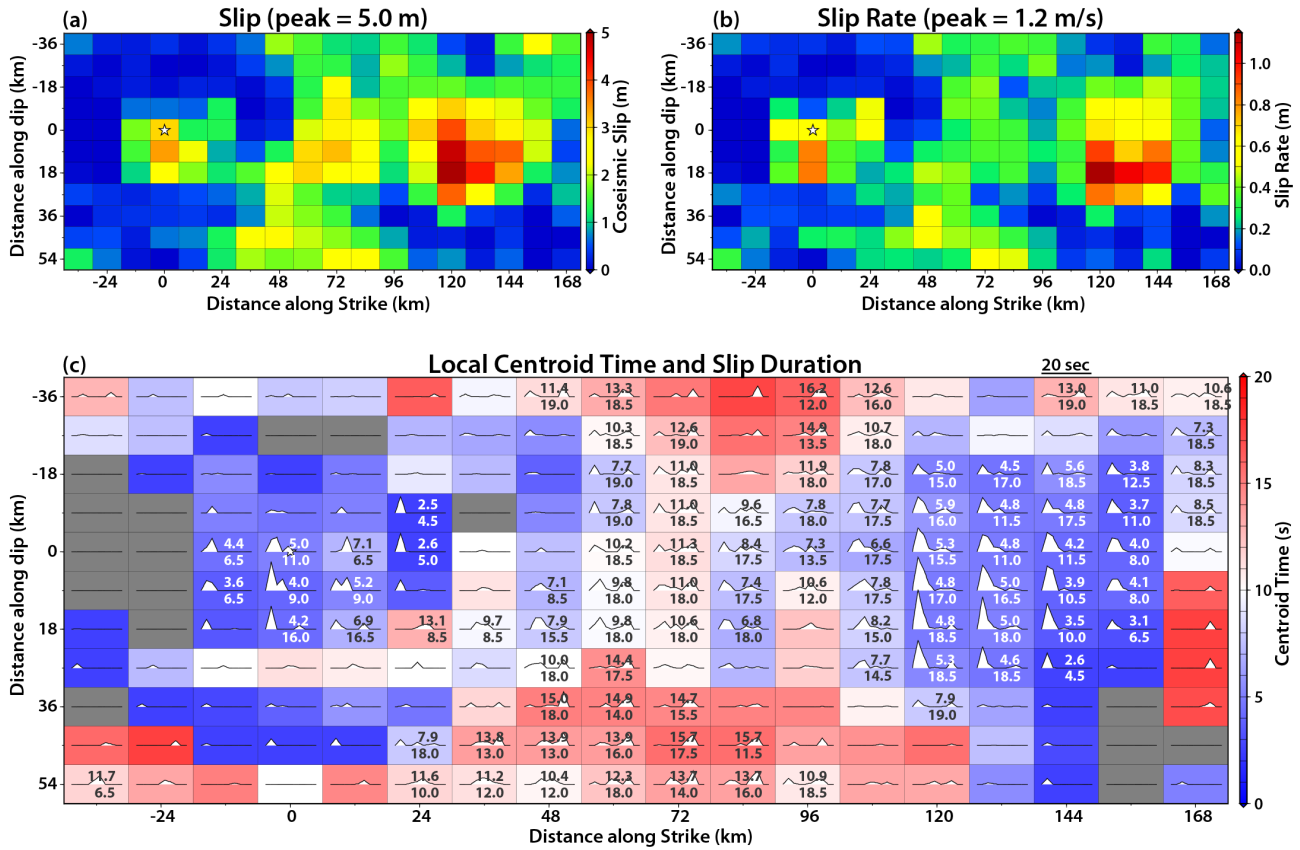
32
33
34
35
36
37
38

Figure S3. Representative W -phase waveform fits for the moment-tensor source in Figure S2. Data (black) and synthetic (red) waveforms are filtered in the period band of 100 to 600 s. Signal in the time window bounded by the two red dots on each trace is used in the inversion. In each insert map, the blue star is the epicenter of the source, the large red circle corresponds to the station with waveform shown to the left and the small gold circles indicate all stations used in the inversion.



39

40 **Figure S4.** Distribution of the slip (a), peak slip rate (b) and local centroid time (c) of our preferred model for
 41 the 2019 M_W 8.0 Peru earthquake shown in Figure 3. Each subfault source time function is prescribed by 18
 42 overlapping triangles with 2 s rise time (half time) shifted by 2 s, resulting in a maximum subfault slip duration
 43 of 38 s. In (c), the subfault source time functions are shown within each subfault by gray polygons. For
 44 subfaults with slip larger than 25% of the peak slip, two values are marked: the top value is the local centroid
 45 time which is average time weighted by the moment rate function, and the bottom value is the local slip
 46 duration during which 2% to 98% of local slip occurs. Due to the large dt and discrete triangles used in the
 47 parameterization of the finite-fault inversion (Ye et al., 2016a), the local duration is not precise.



48

49

50

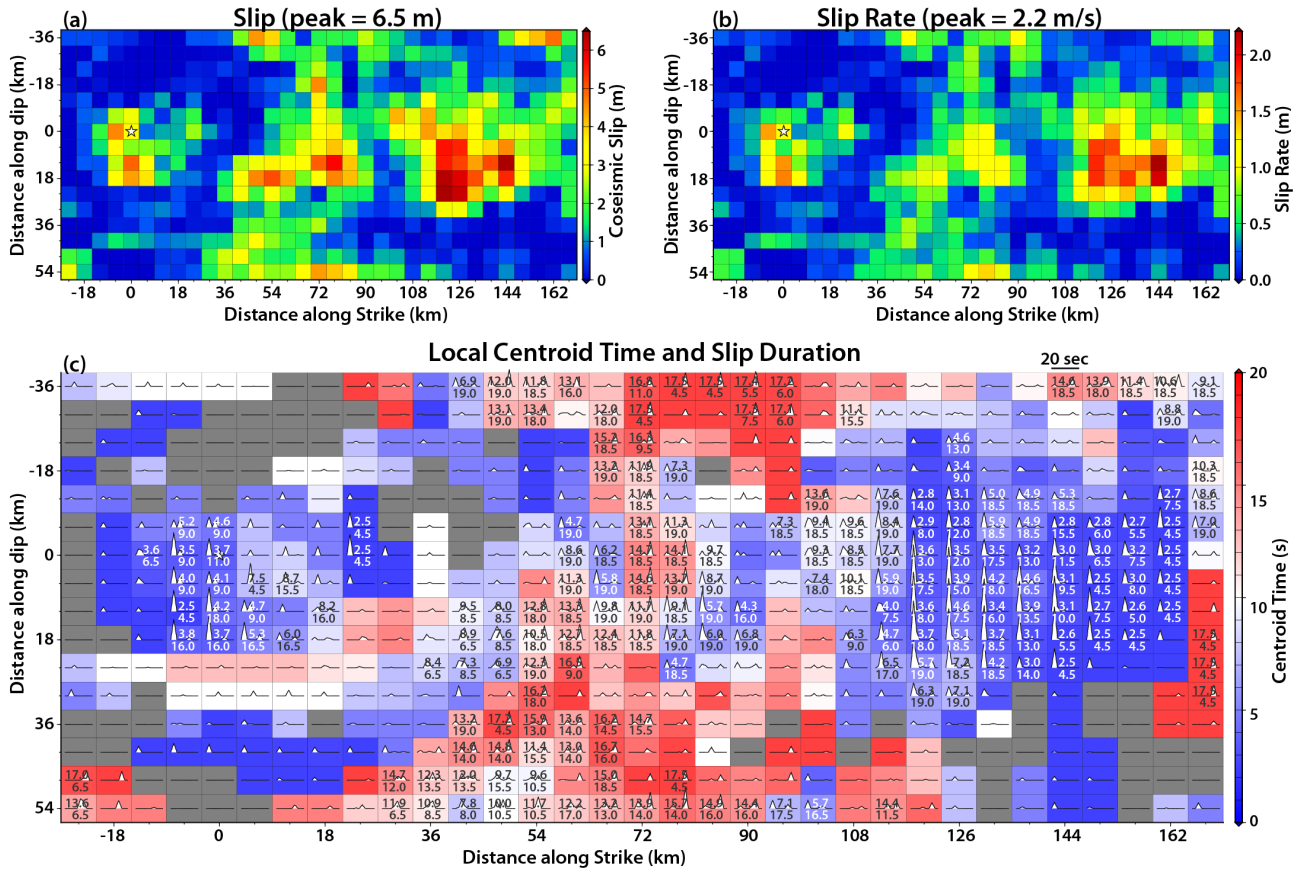
51

52

53

54

Figure S5. Distribution of the slip (a), peak slip rate (b) and local centroid time (c) of an inversion model with relatively short assumed source time function for each subfault for the 2019 M_w 8.0 Peru earthquake. Each subfault source time function is prescribed by 7 overlapping triangles with 2.5 s rise time (half time) shifted by 2.5 s, resulting in a maximum subfault slip duration of 20 s. The grid spacing is 12 km along strike and 9 km along dip, which are the same as for our preferred slip model (Figures 3 and S4). The layout is the same as in Figure S4.



55
56
57
58
59
60

Figure S6. Distribution of the slip (a), peak slip rate (b) and local centroid time (c) for an inversion with small grid size for each subfault for the 2019 M_w 8.0 Peru earthquake. The grid spacing is 6 km along strike and 6 km along dip. Each subfault source time function is prescribed by 7 overlapping triangles with 2.5 s rise time (half time) shifted by 2.5 s, resulting in a maximum subfault slip duration of 20 s, which is the same as for the model shown in Figure S5. The layout is the same as in Figure S4.

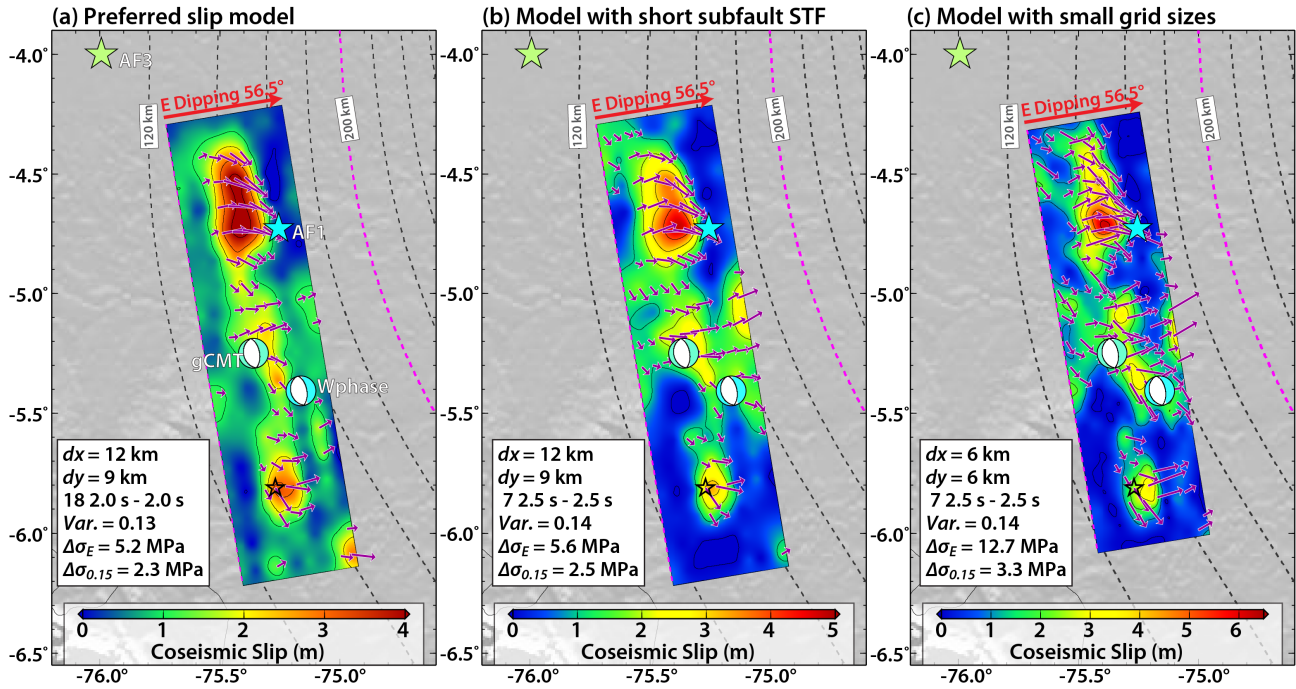
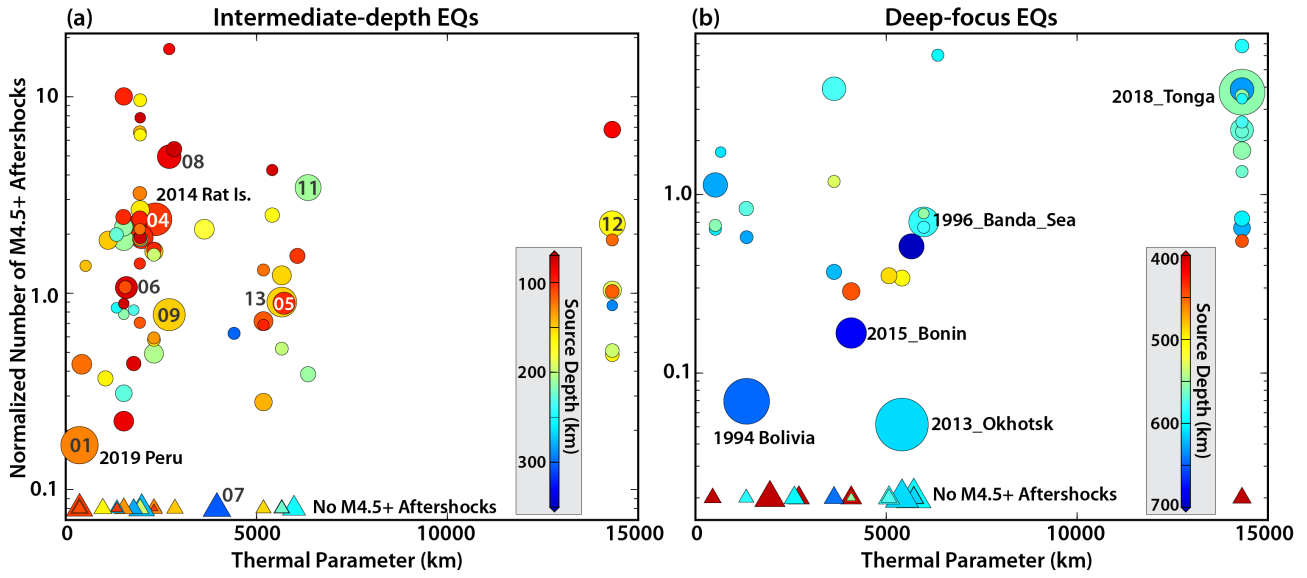


Figure S7. Comparison of (a) our preferred slip model (Figures 3 and S4), (b) the slip model with short assumed subfault source time function (Figure S5), and (c) the slip model with short subfault source time function and small grid size (Figure S6). Other symbols are the same as in Figure 4.

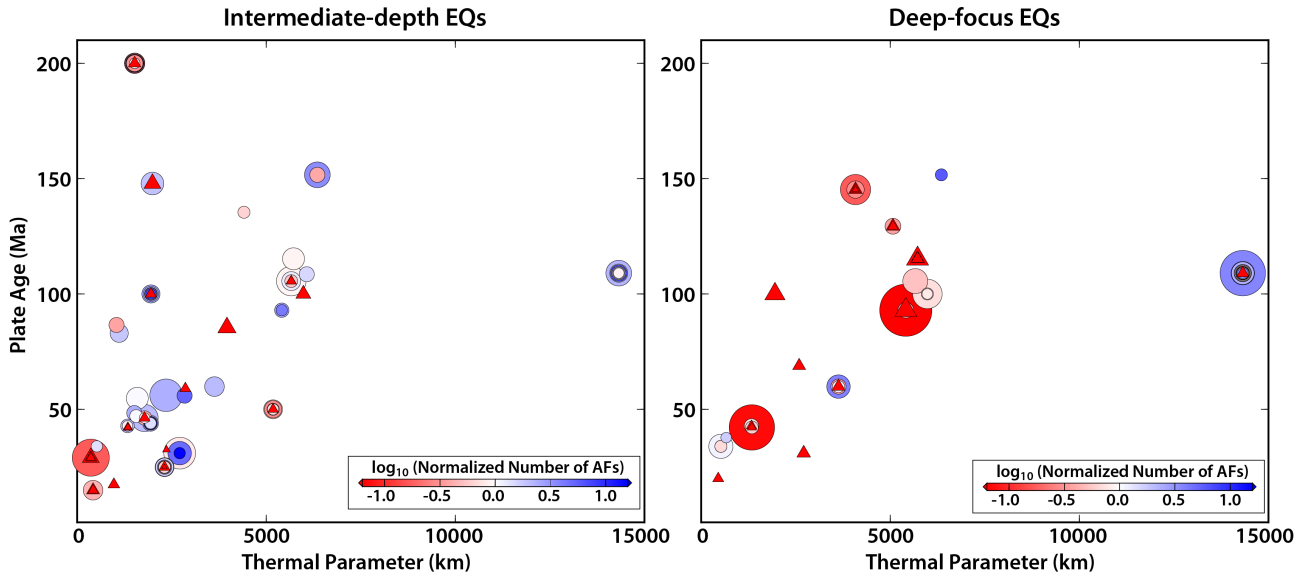


65

66

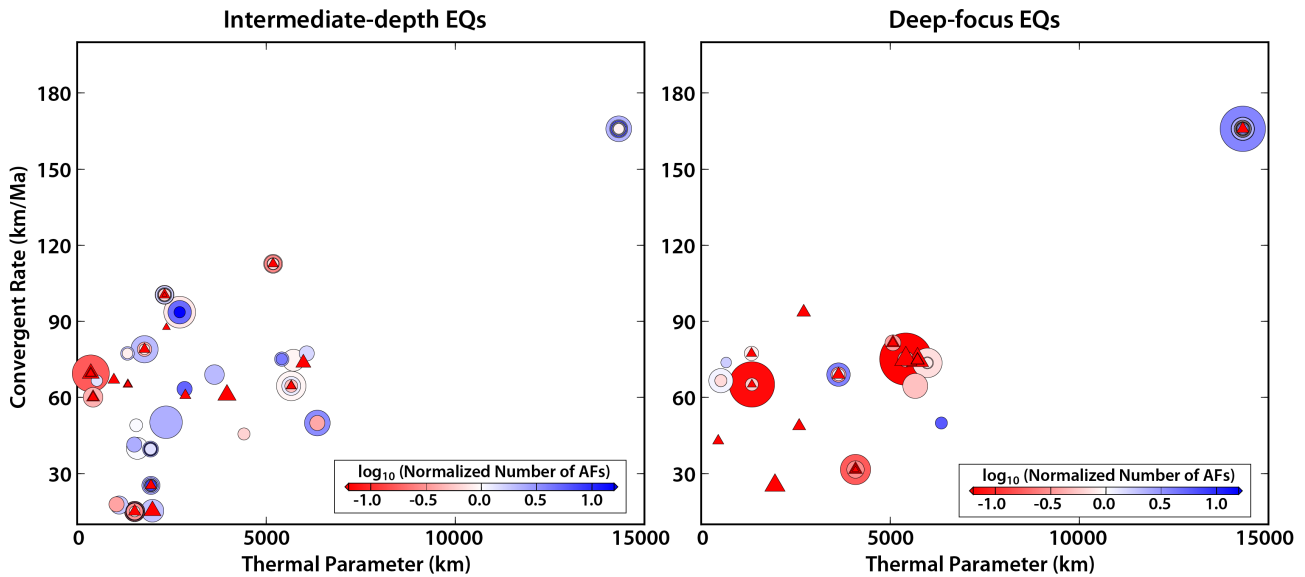
67

Figure S8. Variation of magnitude-scaling normalized number of aftershocks for magnitude larger than 4.5+ for intermediate-depth earthquakes (left) and deep-focus earthquakes (right) with slab thermal parameter.

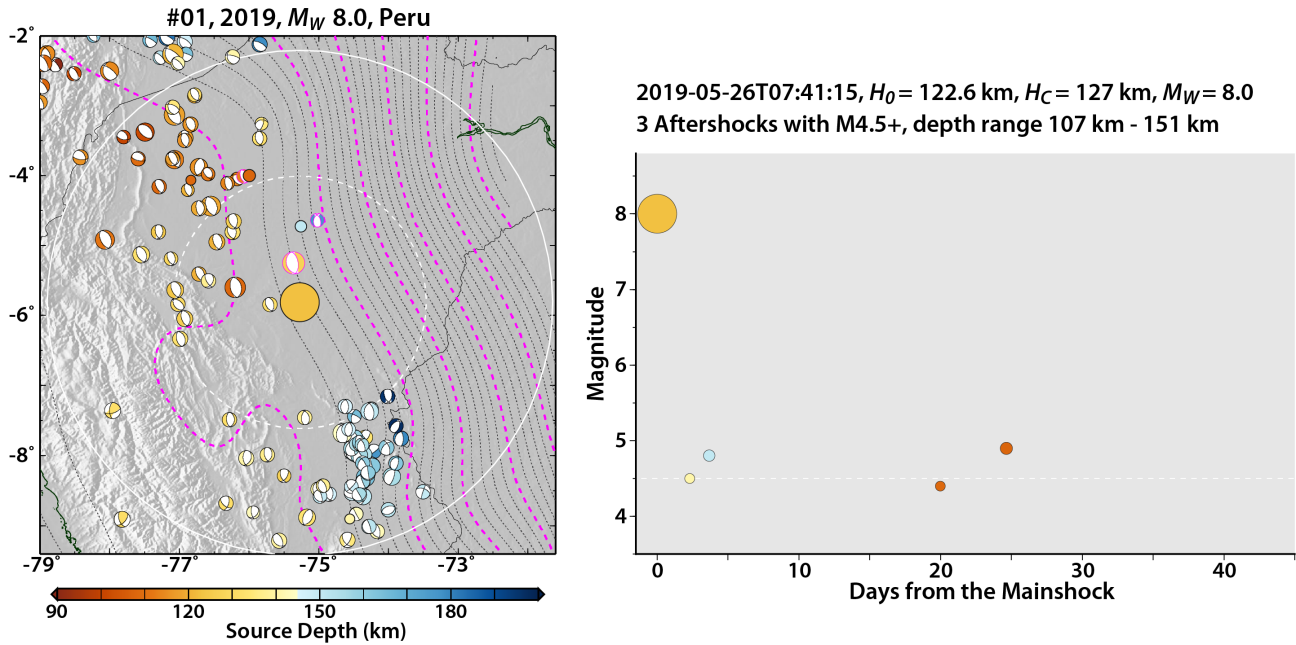


68
 69 **Figure S9.** Plate age versus slab thermal parameter for intermediate-depth earthquakes (left) and deep-focus
 70 earthquakes (right), color coded with the normalized aftershock productivity. Plate age and thermal parameter
 71 are from Syracuse et al. (2010).

72
 73
 74
 75
 76
 77

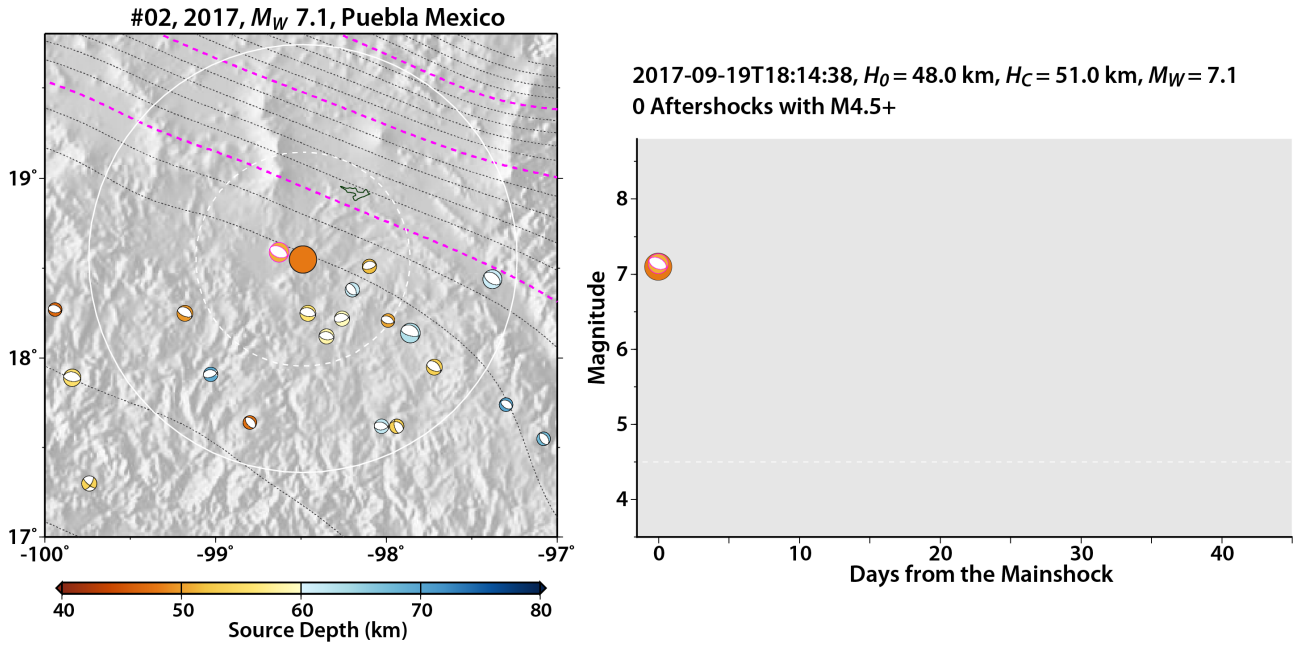


78
 79 **Figure S10.** Convergent rate versus slab thermal parameter for intermediate-depth earthquakes (left) and
 80 deep-focus earthquakes (right), color coded with the normalized aftershock productivity. Convergent rate and
 81 thermal parameter are from Syracuse et al. (2010).



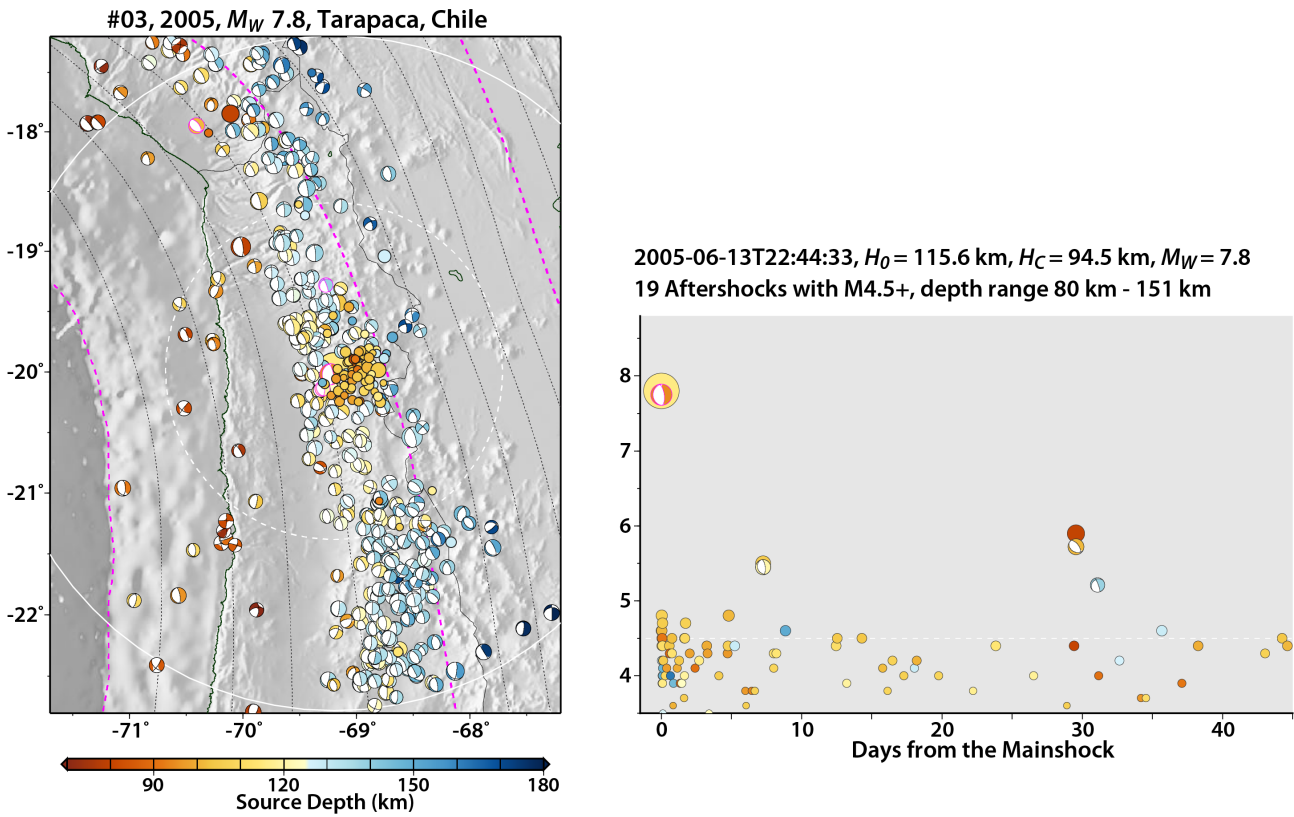
82

83 **Figure S11.** Left: Aftershock activity and background focal mechanisms for the 2019 M_W 8.0 Peru earthquake.
 84 Focal mechanisms from the gCMT catalog for intermediate-depth earthquakes from 1976 to 2019. Aftershocks
 85 within 45 days in the USGS-NEIC catalog (circles) are shown, along with their available gCMT focal
 86 mechanisms with best-double-couple plotted with magenta lines. The black and magenta dashed curves are 20
 87 km and 100 km depth contours of the slab interface from Slab2 (Hayes et al., 2018), respectively. The dashed
 88 white circle has a radius R from the USGS-NEIC epicenter of the mainshock equal to the empirical rupture
 89 length from Wells and Coppersmith (1994). The solid white circle has radius $2R$ and is used for the aftershock
 90 search window. Right: Aftershock time series within 45 days in the USGS-NEIC catalog, plotted from the
 91 origin of the mainshock.



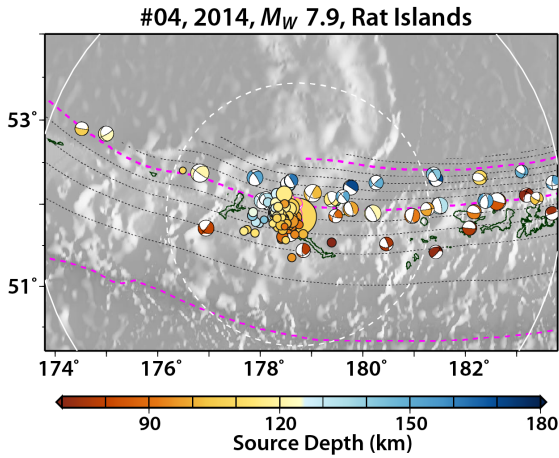
92
93
94
95
96

Figure S12. Left: Aftershock activity and background focal mechanisms for the 2017 M_W 7.1 Puebla, Mexico earthquake. Right: The aftershock time series. Symbols are the same as in Figure S11.

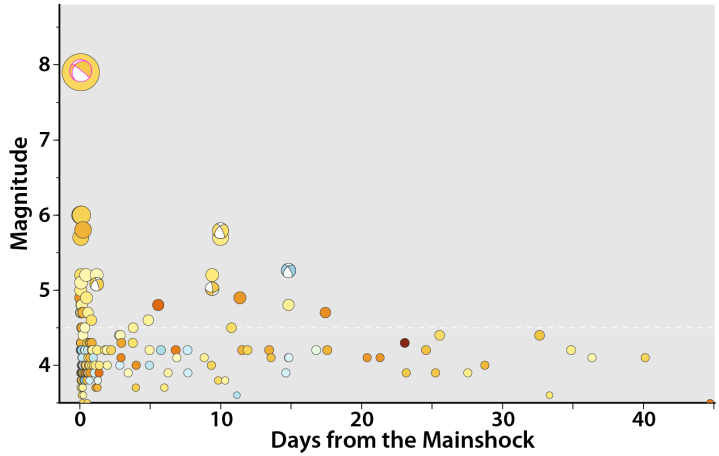


97
98
99

Figure S13. Left: Aftershock activity and background focal mechanisms for the 2005 M_W 7.8 Tarapaca, Chile earthquake. Right: The aftershock time series. Symbols are the same as in Figure S11.

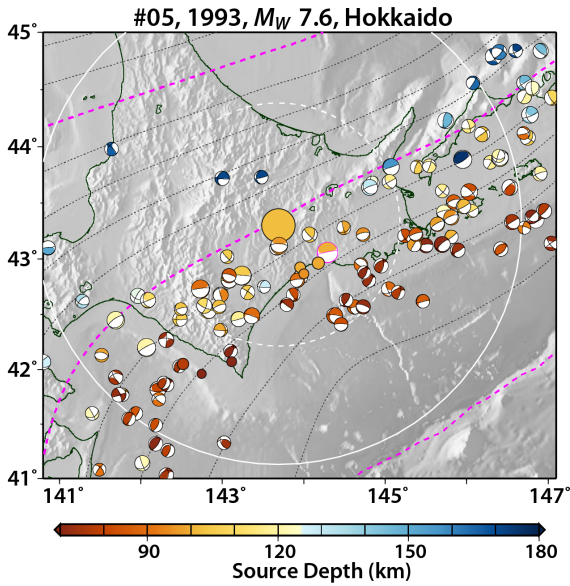


2014-06-23T20:53:10, $H_0 = 109.0$ km, $H_C = 104.3$ km, $M_W = 7.9$
 33 Aftershocks with $M_{4.5+}$, depth range 88 km - 126 km

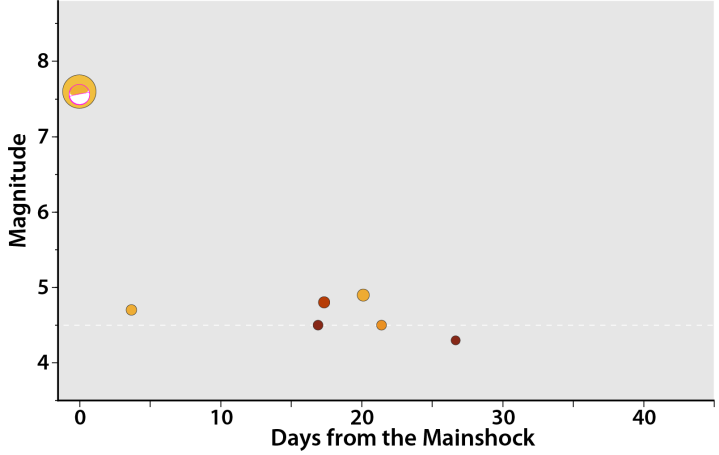


100
 101
 102
 103
 104
 105
 106
 107
 108
 109

Figure S14. Left: Aftershock activity and background focal mechanisms for the 2014 M_W 7.9 Rat Islands earthquake. Right: The aftershock time series. Symbols are the same as in Figure S11.

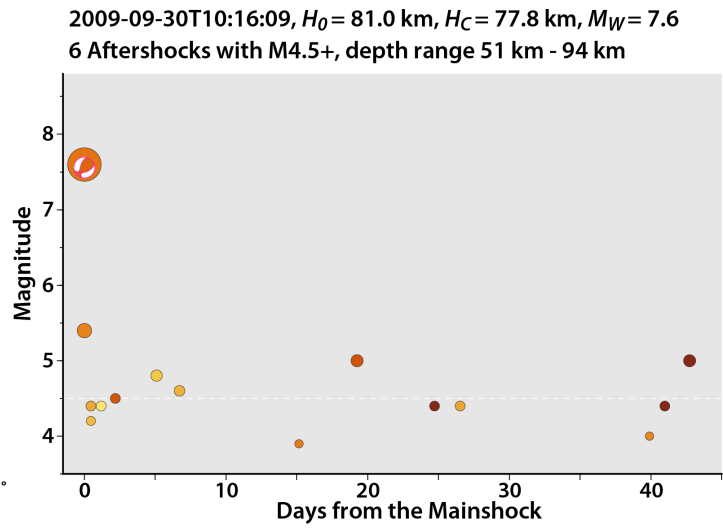
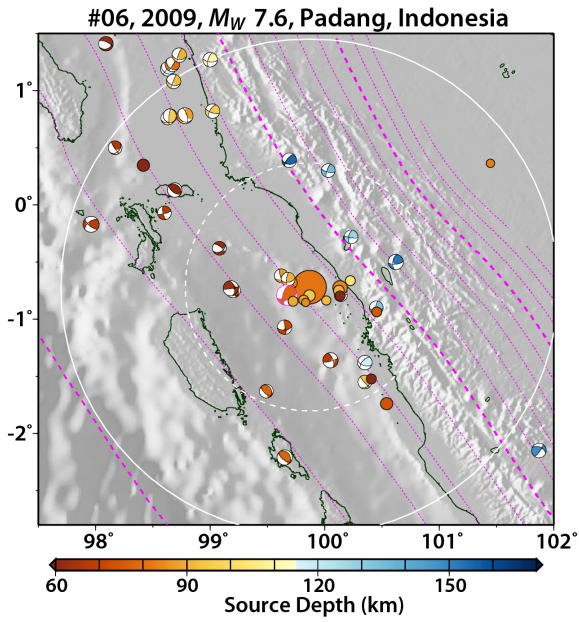


1993-01-15T11:05:06, $H_0 = 102.2$ km, $H_C = 100.0$ km, $M_W = 7.6$
 5 Aftershocks with $M_{4.5+}$, depth range 66 km - 102 km



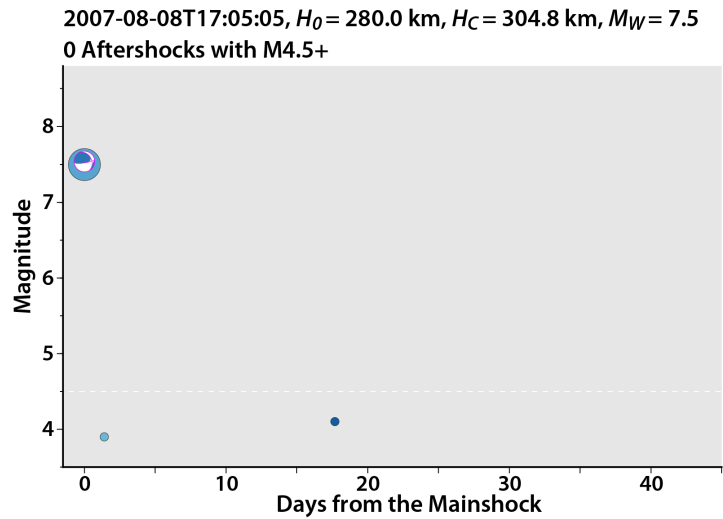
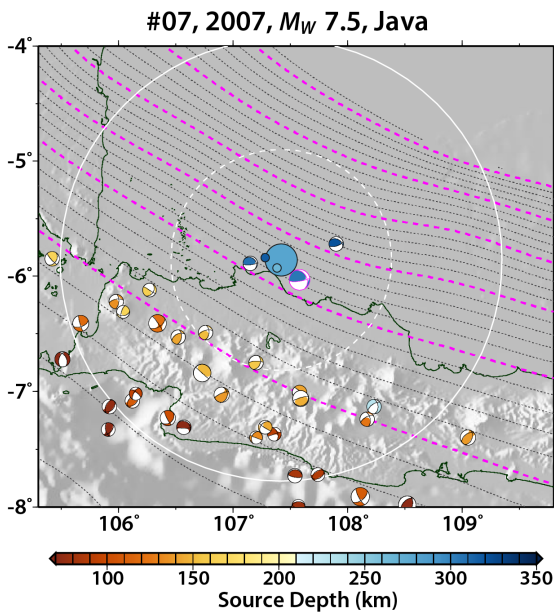
110
 111
 112
 113

Figure S15. Left: Aftershock activity and background focal mechanisms for the 1993 M_W 7.6 Hokkaido, Japan earthquake. Right: The aftershock time series. Symbols are the same as in Figure S11.



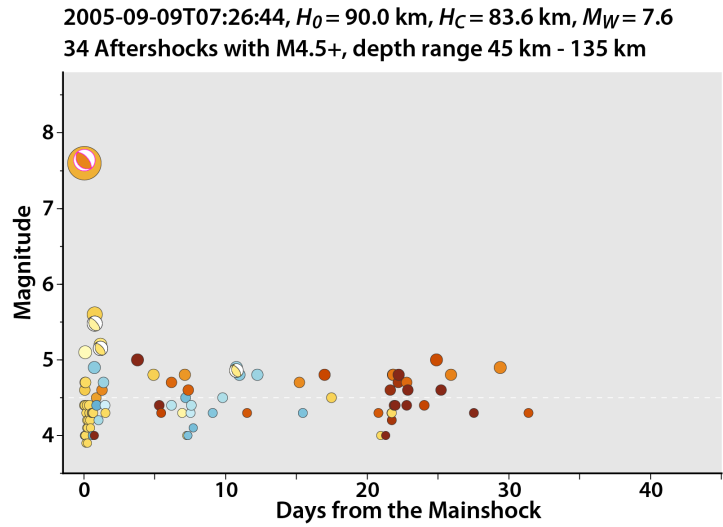
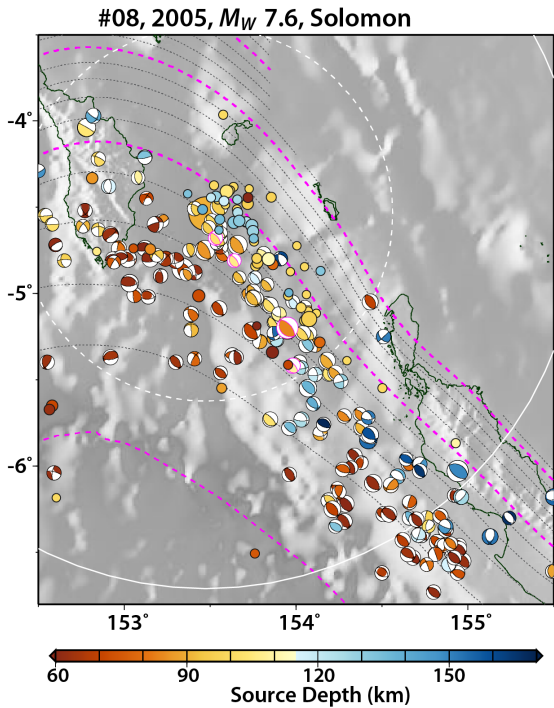
114
115
116
117
118
119
120
121
122

Figure S16. Left: Aftershock activity and background focal mechanisms for the 2009 M_W 7.6 Padang, Indonesia earthquake. Right: The aftershock time series. Symbols are the same as in Figure S11.



123
124
125
126
127

Figure S17. Left: Aftershock activity and background focal mechanisms for the 2007 M_W 7.5 Java earthquake. Right: The aftershock time series. Symbols are the same as in Figure S11.



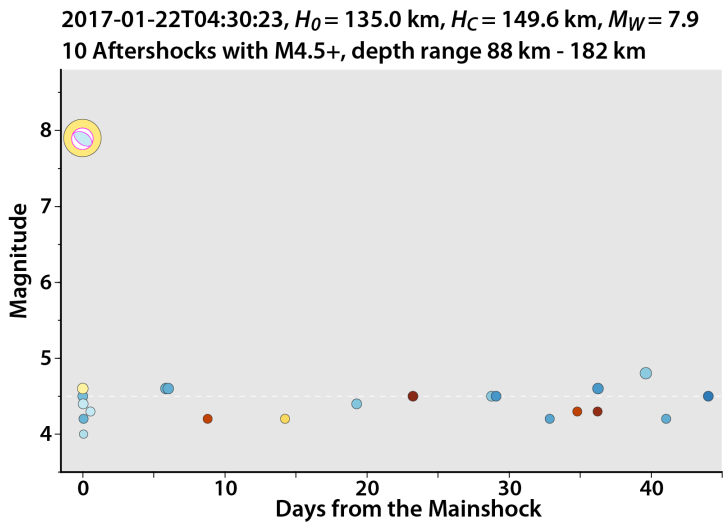
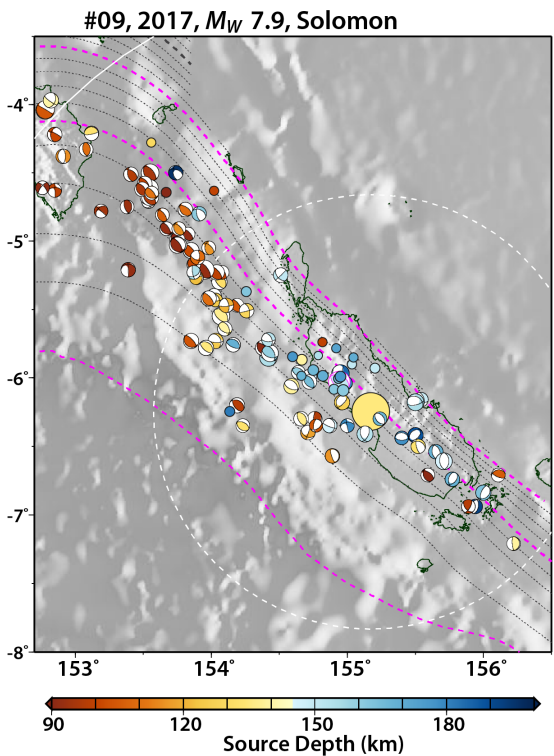
128

129

130 **Figure S18.** Left: Aftershock activity and background focal mechanisms for the 2005 M_W 7.6 Solomon

131

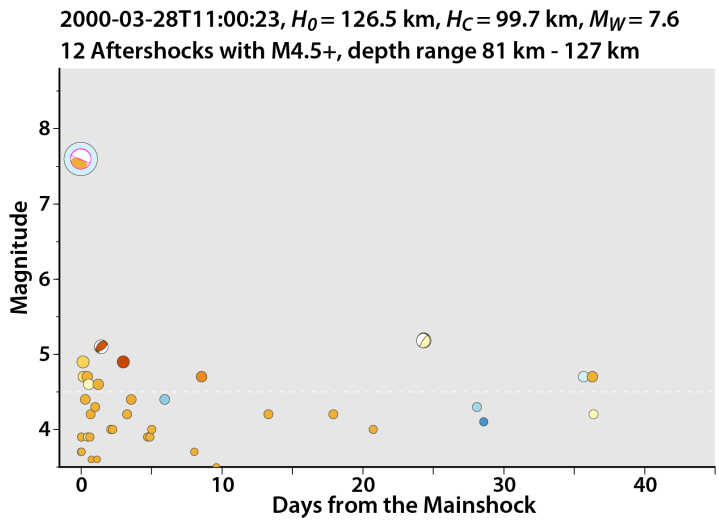
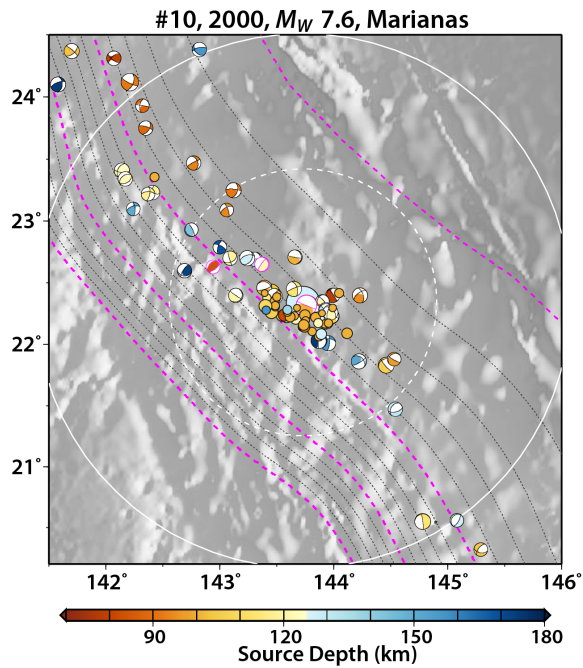
132



133

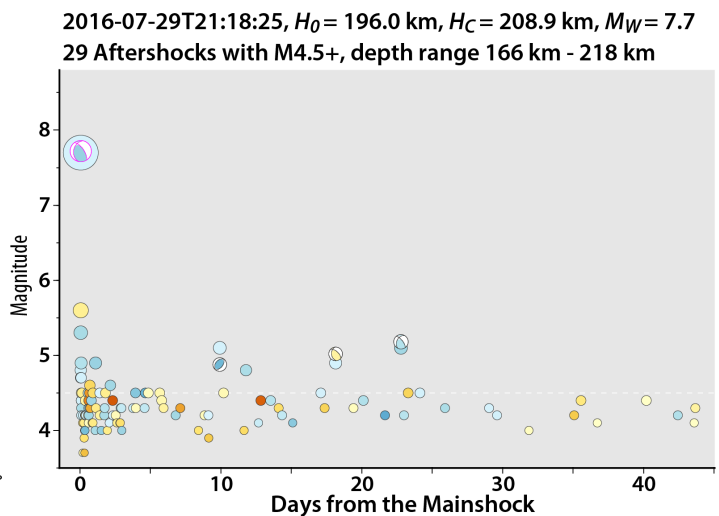
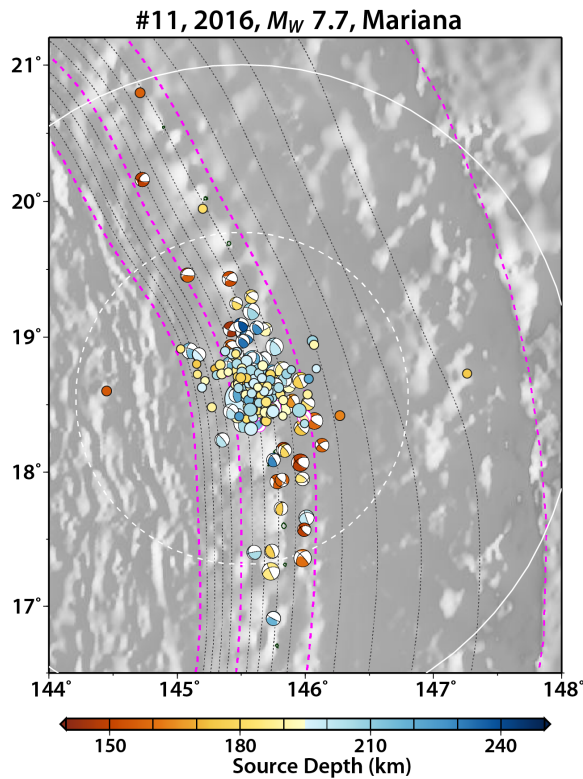
134

135 **Figure S19.** Left: Aftershock activity and background focal mechanisms for the 2017 M_W 7.9 Solomon



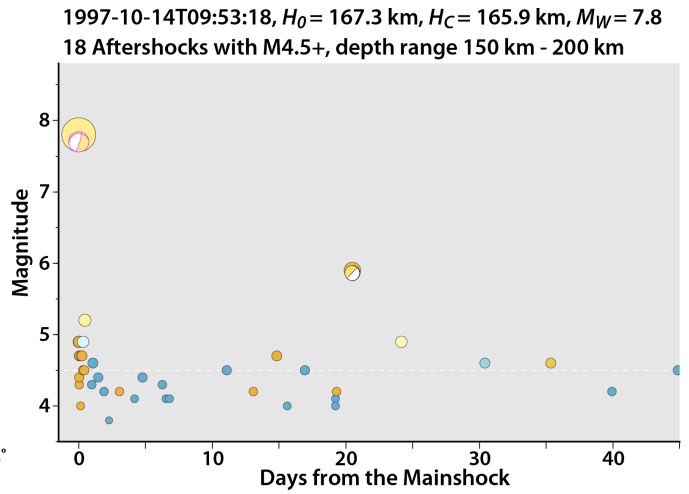
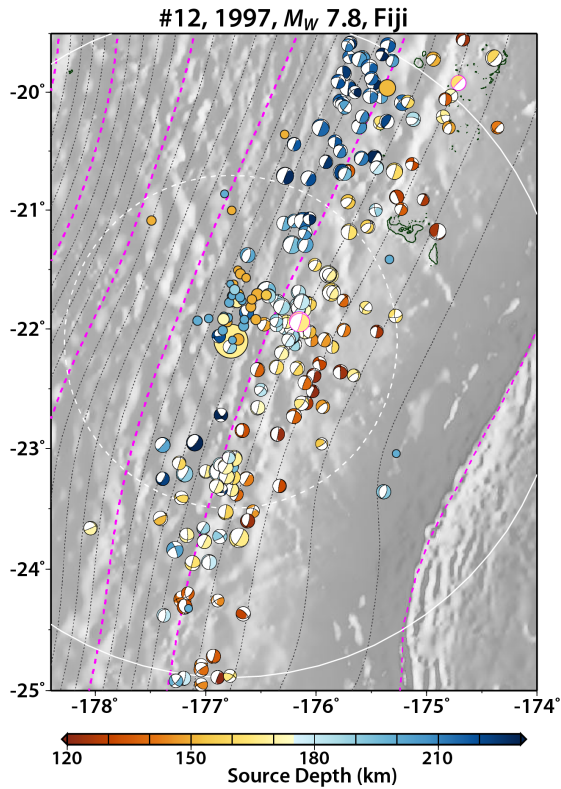
136
137
138
139
140

Figure S20. Left: Aftershock activity and background focal mechanisms for the 2000 M_W 7.6 Mariana earthquake. Right: The aftershock time series. Symbols are the same as in Figure S11.



141
142
143

Figure S21. Left: Aftershock activity and background focal mechanisms for the 2016 M_W 7.7 Mariana earthquake. Right: The aftershock time series. Symbols are the same as in Figure S11.



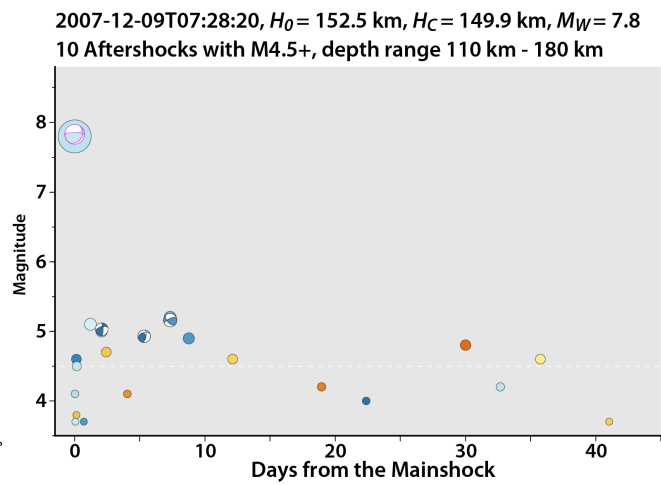
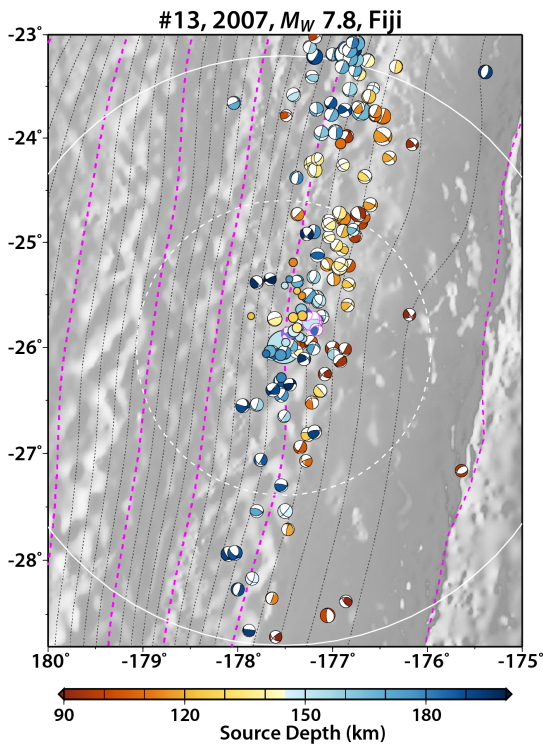
144

145 **Figure S22.** Left: Aftershock activity and background focal mechanisms for the 1997 M_W 7.8 Fiji earthquake.

146

Right: The aftershock time series. Symbols are the same as in Figure S11.

147



148

149 **Figure S23.** Left: Aftershock activity and background focal mechanisms for the 2007 M_W 7.8 Fiji

150 earthquake. Right: The aftershock time series. Symbols are the same as in Figure S11.